Progress in Additive Manufacturing (2025) 10:3335–3360
https://doi.org/10.1007/s40964-024-00808-5

FULL RESEARCH ARTICLE

Elucidating the effects of metal transfer modes and investigating the material properties in wire-arc additive manufacturing (WAAM)

Hambal Iqbal[1] · Alessandro Ascari[1] · Alessandro Fortunato[1] · Erica Liverani[1]

Received: 19 March 2024 / Accepted: 14 September 2024 / Published online: 25 September 2024

Abstract

Studies have shown the influence of WAAM process parameters on mechanical properties, bead formation, dimensional accuracy, and microstructure. However, metal transfer modes and their interactions with input variables have not been investigated thoroughly. Therefore, short/spray, pulse and double pulse modes were investigated in this study at different current levels. Bead-on-plate trials were conducted by depositing ER70S-6 wire to investigate bead morphology, dilution, microstructure, and hardness. The study was supported by a detailed statistical approach, including analysis of variance (ANOVA) and regression analysis. Similarly, the combined effects of hatch distance and current were studied on bead formation in multi-layer deposits. Moreover, a thin wall and a cubic structure were deposited to realize the WAAM capability for larger depositions. The microstructures of thin wall and cubic structure were analyzed using optical microscopy (OM) and scanning electron microscopy (SEM). The study concludes that metal transfer modes at various currents significantly influence bead geometry, microstructure and hardness. The microstructure of bead-on-plate trials show fine lamellar structure at low current in all modes. Higher current results in coarse grains with a polygonal and columnar morphology. The hardness shows a decreasing trend as the current increases. The combined effects of current and hatch distance alter bead morphology; however, an optimized combination yields smoother surfaces. The microstructure of thin wall showed a slight anisotropy along the building direction. The presence of small pores was witnessed from OM and SEM images. Similarly, the cubic structure showed a more homogeneous microstructure with much lower porosity. The hardness profile of the thin wall exhibited small fluctuations along the building direction, while that of the cubic structure was more uniform.

Keywords Metal transfer modes · Additive manufacturing · Arc welding · 3D printing · Wire arc additive manufacturing

1 Introduction

Recently, the field of additive manufacturing (AM) has seen significant advancements, thereby replacing the traditional subtractive processes for many applications. This has also paved the way for hybrid manufacturing [1] which in parallel, combines additive manufacturing process with subtractive manufacturing processes such as turning, milling, grinding, cutting, and drilling. Among additive manufacturing processes, wire arc additive manufacturing (WAAM) has gained remarkable recognition in additive manufacturing community due to its higher material deposition rate, low cost, and flexibility in depositing various materials.

✉ Hambal Iqbal
hambal.iqbal2@unibo.it

[1] Department of Industrial Engineering, University of Bologna, Viale del Risorgimento 2, 40136 Bologna, Italy

WAAM is a directed energy deposition (DED) process [2] among the larger field of additive manufacturing (AM) technology that is based on traditional arc welding. WAAM has different process variants depending on its energy input and the way its feedstock is fed and deposited. Gase metal arc welding (GMAW) [3], gas tungsten arc welding (GTAW) [4] and plasma arc welding (PAW) [5] are the most prominent process variants of WAAM; however, GMAW-based WAAM process stands out due to its fast deposition rate, great mechanical properties, and versatility of materials selection. In its simplest form, a WAAM system is an assembly of a heat source, a wire feeder, and a motion system, most commonly employing a welding robot. An electric arc is sustained between the tip of the wire electrode and base metal, thereby melting, and depositing the metal wire layer-by-layer to form a 3D structure. A shielding gas is usually used to protect the arc and to help in smooth transfer of molten metal droplets during the WAAM process. The

persistent study of AM researchers for efficiency, customization and cost-effectiveness has led to the development of WAAM. The integration of GMAW with robotic systems further increases the precision and control in the layer-by-layer WAAM process, extending its applications in various industries, including aerospace [6], automotive [7], and construction [8]. Unlike conventional manufacturing processes, WAAM enables near net shape direct manufacturing of complex and large components, hence offering a customized and rapid approach to production.

WAAM technology can deposit various important engineering materials such as titanium alloys [9–11], aluminum alloys [12–14], nickel alloys [15, 16] and steel [17, 18]. Compared to subtractive manufacturing, WAAM can reduce the fabrication time by 40–60% and post-machining time by 15–20% depending on the component size [19]. Similarly, the energy needed to fabricate WAAM components is 85% less than in the powder-based additive process [20]. Not only that wire feedstock is more economical than powder feedstock [21] but also using wire as feedstock eliminates the use of powder recycling processes [22]. Moreover, the high deposition rate of 5–6 kg/h [23] makes it a promising technology for large structures. Therefore, WAAM has gained huge popularity among additive manufacturing researchers due to its many advantages.

Although the WAAM process is based on traditional welding technology, the desired outcomes are different than those in welding. As shown in Fig. 1, deep penetration and low reinforcement height is desirable in welding to fill the joint between two metal parts or to fuse them overlapped, while in additive manufacturing, it is desirable to have a lower penetration and higher layer height. In traditional welding, deep penetration is desirable to ensure a strong fusion and hence durability and structural integrity, but a lower weld height is needed for a smooth and seamless joint. On contrary, the additive manufacturing demands a lower penetration in the substrate or previously deposited layers to avoid the excessive heat input and the potential residual stresses, while a higher reinforcement height is necessary in the layer-by-layer process to ensure a controlled material buildup. This is very crucial for additive manufacturing where a layerwise deposition is carried out to manufacture a complex product. Therefore, in conventional welding process, priority is given to joint strength and fusion depth, while in additive manufacturing, a controlled layering is needed for a precise deposition of a complex structure and at the same time ensuring the structural integrity of the product and avoiding the excessive heat which not only alters the mechanical properties but may also jeopardize the geometrical accuracy of the additively built structures. Therefore, it is important to understand and realize these differences to optimize the WAAM process parameters and provide the intended results. To obtain optimal performance in terms of structural integrity, surface finish, and overall quality, careful inquiry is required into the intricate interactions between variables such as welding parameters, deposition speed, and hatch distance to mention a few. Similarly, the characteristics of the geometry are linked to the process parameters [24]. The layer wise deposition in WAAM causes heat accumulation which in turn modifies the bead morphology, microstructural characteristics and hence the mechanical properties. The main parameters directly responsible for heat input are deposition current, voltage, travel speed (TS), and wire feed speed (WFS) which cumulatively vary the heat input and ultimately the other properties [25–27]. The ratio of WFS/TS is the most significant process parameter for controlling heat input where heat input influences the bead dimensions, including weld width, weld height, penetration depth, penetration area, and reinforcement area [17]. Moreover, cyclic heating and uneven solidification rates from the center of each melt-pool towards solidified regions results in contrasting microstructures [28] and grain size [29]. The voltage and the travel speed significantly affect the bead width, while the travel speed and welding current have evident influence on the bead height [30].

Another important aspect in WAAM deposition is the metal transfer mode [31, 32]. WAAM is useful in high deposition metal additive manufacturing, which usually

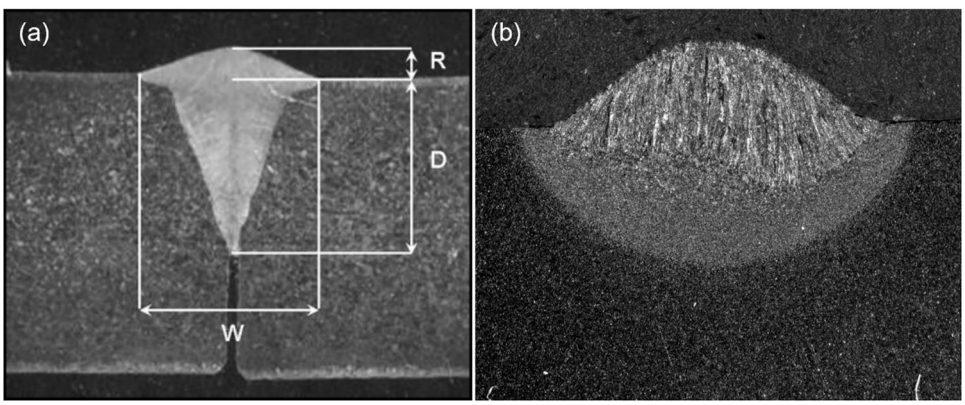

Fig. 1 **a** Deep penetration in welding [37], **b** partial penetration in a single-track WAAM deposit

corresponds to high heat input that can cause geometrical inaccuracies, lower surface finish and other metallurgical concerns. However, such problems can be resolved with high performance metal transfer processes. For example, controlled short-circuiting metal transfer process with modified waveforms improves geometry preservation stability at high process rates [33]. Similarly, for multi-bead deposition, suitable overlapping distance between adjacent beads can minimize the valleys between layers [34]. Hence, selection of optimal hatch distance is also significant. Daniel Ramos-Jaime et al. [35] designed a three factors three levels experiment with a single replicate to study the effect of wire feed speed, welding speed and welding voltage on bead cross section. In this study, they concluded that the factors under study influence the bead area in gas metal arc welding (GMAW) process. They also developed a mathematical model to predict the effect of process parameters on bead dimensions within 0 – 20% accuracy. Paul et al. [36] varied the travel speed (mm/s) and eventually the heat input (j/mm) while keeping voltage and current constant to deposit ER70S-6 wire with a Fronius (TPS320i). They found that an optimal heat input exists to reduce deposition time.

WAAM technology is still pre-mature and needs comprehensive studies to unleash the complex process. Many researchers have investigated the process parameters for individual metal transfer modes. However, there is a lack of studies in the literature that elucidate these parameters across different metal transfer modes with a comparative approach based on detailed statistical analysis. Moreover, the existing literature usually covers only the bead shapes. Therefore, this study investigates various metal transfer modes to realize their influence and interactions with the deposition current on bead characteristics, dilution, macro and microstructure and microhardness. Similarly, the combined effects of hatch distance and current are investigated on bead formation in multi-bead deposits. Eventually, the work was extended to understand the microstructural evolution and hardness profiles for larger scale structures. Hence, this study seeks to contribute to valuable insights into these knowledge gaps.

The following sections will present the materials and methods, explaining the methodology, experimental design, and scientific approaches utilized in this work. Next, the results and discussions will provide a critical assessment of the findings. Finally, the conclusions will highlight the most significant discoveries.

2 Materials and methods

The experiments were performed using a synergic controlled GMAW-based heat source (Selco Genesis 352 GSM), integrated with a wire feeder (Selco WF104), in direct current electrode positive (DCEP) polarity. The path planning was executed by a 6-axis welding robot (Yaskawa Motoman HP20). The WAAM setup is shown in Fig. 2. The welding torch was moved precisely by the robot arm to deposit successive layers of molten material on a mild steel substrate, while the wire was continuously supplied by the wire feeder and fused across the arc generated by the welding source. The wire feedstock used for the deposition was AWS A5.18 ER70S-6 with a diameter of 1.2 mm. The chemical composition of wire is reported in Table 1. To prevent the process from oxidation and ensure a good quality deposit during the WAAM process, argon with 20% carbon dioxide was used as shielding gas at a flow rate of 18 l/min. In the first part of the experiment, bead-on-plate tracks were deposited using three levels of deposition current and three different metal transfer modes. The current levels used included 100, 200 and 300 A in short/spray transfer mode, pulse mode and double pulse transfer mode. These input variables were set on the WAAM heat source before depositing the corresponding beads. The travel speed (TS) was kept constant at 11 mm/s

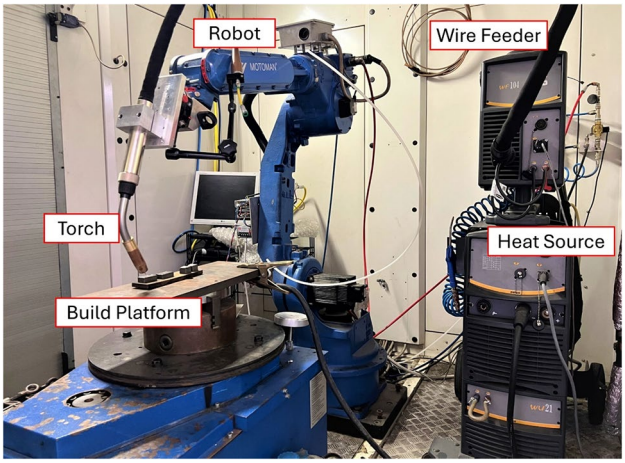

Fig. 2 WAAM process experimental setup

Table 1 Chemical composition of ER70S-6 [38]

Constituents	Mass %
C	0.06–0.15
Si	0.8–1.15
Mn	1.4–1.85
P	0.025 max
S	0.035 max
Ni	0.15 max
Cr	0.15 max
Mo	0.15 max
Cu	0.5 max
V	0.03 max
Fe	Bal

of robot movement, while the voltage and wire feed speed (WFS) were obtained on the screen of synergic controller based on the nominal input current. The input variables with calculated heat input are shown in Table 2. These parameters were selected to incorporate a range of heat input for each metal transfer mode. The response variables include the bead morphology, macrostructure, microstructure, microhardness, and dilution of single beads. Heat input was calculated based on the actual current obtained on the synergic controller from the formulae shown in Eq. 1. After the deposition, samples were cut using a metallographic cutting machine (Remet TR60). Bead-on-plate tracks were cut at 3 different sections (i.e., top, middle and end) and a total of 27 samples were prepared. All the specimens were mounted on resins and polished on a polishing machine (Remet RS2) from 80 – 2500 abrasive grits, followed by polishing with diamond spray of 6 and 1 microns, respectively. For macro- and microstructural analysis, the samples were etched with 4% Nital and analyzed with an optical microscope (Carl Ziess Stemi 508 doc). Macrostructural images were obtained from a macroscope (Vert.A1 Ziess Axio). Similarly, to assess the mechanical properties, microhardness tests were performed on a Vickers hardness tester (Leitz) for a load of 1 kg and an indentation time of 15 s. After the data were collected, the statistical analysis was performed using Python 3.12 in visual studio code editor. The data were imported utilizing the Pandas library, while the Statsmodel library was used for ANOVA and regression analysis.

$$\text{Heat input}\left[\frac{\text{J}}{\text{mm}}\right] = \frac{I * V}{TS} \tag{1}$$

The second part of the experiment was conducted by depositing multi-bead samples at various current levels and hatch distances between the adjacent beads to study their combined effects on bead morphology. For these samples, a hatch distance of 2, 3 and 4 mm were repeated 3 times each for 80, 120 and 160 A current in pulse transfer mode. Hence, nine samples were obtained to analyze the combined effects of current and hatch distance on bead formation. All the deposited multi-bead samples were cut in the middle, perpendicular to the deposition direction for further analysis.

The third part of this study consists of depositing a thin wall for realizing WAAM's capability for larger structures. The thin wall consisted of ten stacked layers in which all the layers were started and ended from the same point, i.e., in a parallel deposition strategy. In addition, pulse transfer mode was used with a deposition current of 150 A and with a constant travel speed of 11 mm/s, controlled by robot movement.

Finally, a cubic structure was deposited with 100A current in pulse transfer mode with a deposition speed of 11 mm/s. The hatch distance between the adjacent beads was maintained at 4 mm. An optimized deposition strategy was adopted for the deposition of cubic structure for homogeneous heat distribution. The strategy deposits a single pass shell as the outer perimeter of the cubic structure followed by zigzag infill passes inside the perimeter. For each successive layer, the starting point of deposition head was rotated 90^{o} clockwise for the outer shell and infill passes.

At the end of each layer, the material was left to cool down to room temperature before starting the subsequent layer. After the deposition, the samples were cut extracted from the structures in the middle section along the building direction. For sample preparation, the same metallographic approaches for cutting, polishing, and etching as used in previous sections were applied. Similarly, same hardness equipment and microscope were used for microstructural analysis and hardness tests. For further microstructural characteristics, scanning electron microscopy (SEM) was performed with a Tescan Mira3 SEM machine.

Table 2 Process parameters of bead-on-plate depositions

Metal transfer mode	Nominal current (A)	Voltage (V)	WFS (m/min)	TS (mm/s)	Heat input (J/mm)
Short/Spray	100	16.7	2.1	11	158
Short/Spray	200	20.7	5.4	11	369
Short/Spray	300	28.5	9.3	11	757
Pulse	100	22	2.7	11	116
Pulse	200	26.7	6.4	11	417
Pulse	300	29.7	10.4	11	751
Double pulse	100	22	2.7	11	116
Double pulse	200	26.7	6.4	11	417
Double pulse	300	29.7	10.4	11	751

3 Results and discussion

After the depositions were concluded, a detailed analysis on the collected data was carried out to understand the complex WAAM process. The discussion is comprised of quantitative and qualitative aspects to understand the experimental findings. In the following sections the results are discussed in detail.

3.1 Bead-on-plate analysis

Figure 3(i and ii) shows the as-deposited beads and cross-sectional images taken in the middle section of each sample. It is obvious to identify the shape characteristics for each transfer mode at various current levels. The choice of process parameters and metal transfer modes depends on the end user and specific applications. For example, in additive manufacturing a lower penetration could be desirable that is sufficient to ensure the structural integrity of the build instead of a very deep penetration which causes more heat accumulation in the layer-by-layer process. The short circuit mode at low current level seems to produce a small bead with minimal penetration, which increases with higher current. This could be attributed to the transition between the transfer modes from short-circuiting to spray mode. That is because, at lower current, the standard metal transfer mode employs a short-circuiting transfer mode in which the current is not sufficient to detach the droplet owing to lower electromagnetic forces. The driving force for droplet detachment becomes the surface tension when the wire touches the melt-pool. However, at high current, the metal transfer mode changes to spray transfer. This in turn, changes the arc behavior, heat input and the melt-pool, leading to a deeper penetration. Moreover, pulse and double pulse modes also seem to yield a deeper penetration at high current level. The reason that a lower penetration is desirable in additive manufacturing is to avoid remelting deep within the previously deposited layers. The reason is the corresponding heat accumulation and a possible tempering effect which can alter the microstructure, mechanical properties and induces residual stresses. However, the penetration should be deep enough to ensure the structural integrity of the components under manufacturing. The pulse and double pulse modes seem to have produced an acceptable compromise between the reinforcement height and penetration. However, for high level of current the penetration is too much for additive manufacturing.

In short, it is crucial in additive manufacturing to achieve an optimal balance between the penetration, height and width in multilayer deposits. Therefore, understanding the bead morphology of single beads is crucial, since they act as building blocks for larger structures. Short/spray mode at low current produces shallow penetration and moderate height that can be useful for achieving layer uniformity. However, the reduced bead width in this mode decreases the overall bead size, potentially lowering the material buildup rate for larger structures. Similarly, high current level shows a deep penetration with respect to its height. This can be detrimental for large structural deposits due to excessive remelting, potentially causing a tempering or annealing effect on the previously deposited layers, inducing high residual stresses. Research indicates that increased residual stresses

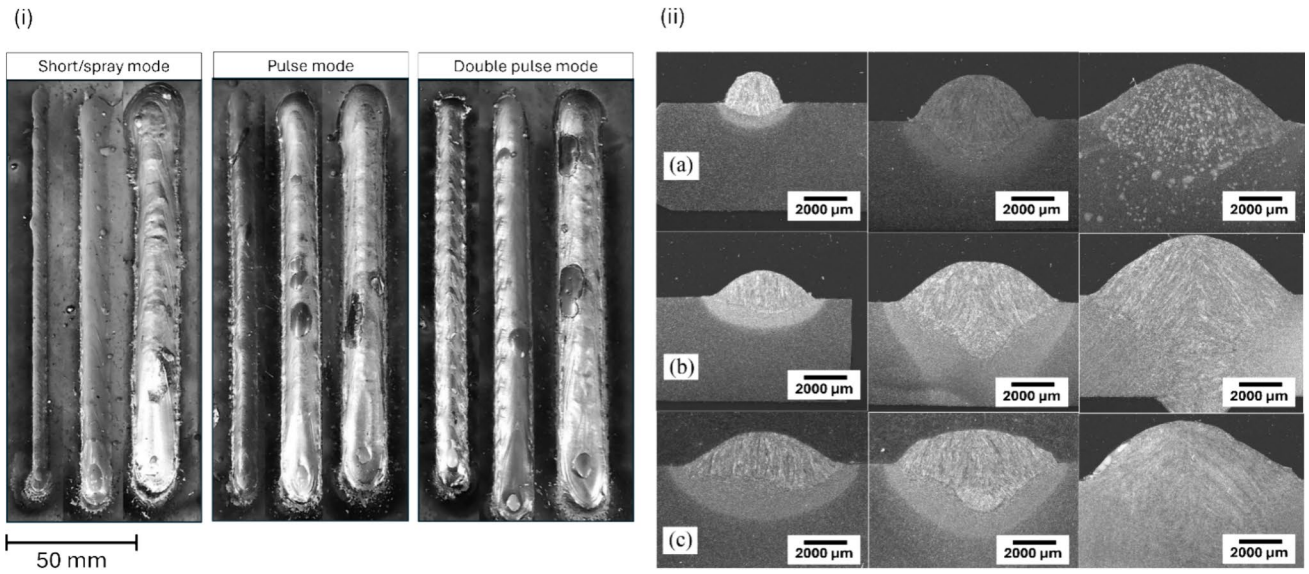

Fig. 3 (i) As-deposited beads at 100, 200, and 300 A (left to right), (ii) macrostructural images (middle section) at 100, 200, and 300 A (left to right): **a** short/spray mode, **b** pulse mode, **c** double pulse mode

alter the microstructure, results in cracking and distortion in large structures [39]. Conversely, pulse and double pulse modes show larger bead widths at low current compared to short/spray mode without affecting the penetration. This characteristic can be desirable in additive manufacturing. Additionally, a reasonable balance between the bead width, height and penetration exists at intermediate current level for both pulse and double pulse modes. However, significantly higher penetration results at high current which is not desirable.

From the visual interpretation it seems that intermediate current in short/spray transfer mode and lower to intermediate current in pulse and double pulse transfer modes can produce optimal bead shapes. This ensures a sound structure with an expected smoother and efficient buildup, which is desirable for larger structures. Apart from the visual interpretation of the macrostructural images, statistical analysis is performed in the next section to reveal such effects and interactions in detail.

An analysis of variance (ANOVA) was performed using a general linear model (GLM) with 95% confidence interval, and the corresponding results are summarized in Table 3. The "Mode" in ANOVA table represents the metal transfer modes. In short, the sum of squares (sum_sq) represents the variability of data and helps in determining the contribution of an independent variable against a dependent variable. Consequently, a higher sum of squares represents a larger contribution of the independent variable.

The ANOVA analysis was performed for penetration, width, height, and hardness to be the response (dependent) variables, while deposition current and metal transfer modes were taken as input (independent) variables. The statistical significance was checked for each response variable against the individual input variables and their interactions by analyzing the *P* values. The ANOVA analysis revealed the statistical significance of all response variables against individual input variables except the height. However, in practice, we assume a direct correlation of height with deposition current. It is possible that the statistical insignificance of height against the input variables corresponds to process instability during WAAM deposition. We have discussed the potential reason in the following section. Moreover, the interaction terms of transfer mode and current is significant for width and hardness but shows no significance for penetration and height.

Following the ANOVA analysis, a detailed regression analysis was also conducted in Python using the statsmodels library, which is based on the Ordinary Least Squares (OLS) method. The regression model includes the main effects of current and metal transfer mode, being the input variables (hereafter referred to as "current" and "mode"). It also includes the interaction terms of these input variables.

Table 3 ANOVA table: showing significance of transfer mode and current on bead penetration, width, height and hardness

Penetration				
	Sum_sq	Df	F	*P* value
Mode	6.311	2.0	5.29	0.016
Current	48.058	2	40.27	0.000
Mode × Current	2.912	4	1.22	0.337
Width				
	Sum_sq	Df	F	*P* value
Mode	11.64	2.0	3.52	0.05
Current	87.64	2.0	26.5	0.000
Mode × Current	25.89	4	3.91	0.019
Height				
	Sum_sq	Df	F	*P* value
Mode	0.379	2.0	0.30	0.745
Current	3.179	2	2.51	0.110
Mode × Current	3.0745	4	1.21	0.340
Hardness				
	Sum_sq	Df	F	*P* value
Mode	2525	2.0	4.65	0.024
Current	11,118	2	20.47	0.000
Mode × Current	3856	4	3.55	0.026

The model formula for each response variable is specified in the following equation:

$$Response \sim C(mode) + C(current) + C(current) : C(mode) \quad (2)$$

In the equation, C(…) represents the categorical encoding of input variables. While the ANOVA analysis revealed the significant factors for each response variable and their interactions, the regression analysis highlighted a more nuanced and detailed understanding of such relationships by providing the estimates of effect sizes and interactions between the factors at each level. The double pulse and 100 A current were automatically selected alphabetically/numerically as baseline in the regression analysis, serving as reference points. This selection provides an explicit comparative analysis between different metal transfer modes and current levels, allowing a clear interpretation of how each input variable effects the response variables. The results of regression analysis for the response variable and their interactions are reported in Table 4 and Table 5, respectively. The tables summarize the statistical metrics for each variable/interaction at various levels with respect to the baseline. The metrics include the coefficient, standard error, *P* value, and confidence intervals. The coefficient represents the effect size, quantifying the expected changes in the corresponding response variables with respect to the baseline. The intercept shows the predicted value of the respective response variables at baseline, i.e., at 100 A in double pulse transfer mode. The standard error is the standard deviation of the coefficient. Similarly, the *P* value represents the significance of the factors at a certain level, indicating whether the results are likely due to chance. The lower and upper bounds of the confidence intervals provide more detailed information than *P* values alone. They estimate that the effect size (coefficient) lies between the upper and lower bounds with 95% confidence.

The regression analysis showed thorough and important findings to underscore the individual main effects and the interaction of input variables on bead morphology and hardness at various levels. For instance, the baseline value for penetration resulted in 1.22 mm at a *P* value of 0.013. When the current is increased to 300 A, the penetration increases by 3.34 mm with respect to baseline value with a *P* value less than 0.001, indicating a direct relationship of penetration with current. The current and mode do not show significant interactions, suggesting that beyond the influence of current, the mode alone does not greatly affect the penetration. This result agrees with ANOVA analysis. Moreover, the baseline value for the width resulted in 7.59 mm. At 300 A, it increased by 2.42 mm, making the width to around 10 mm at this current level. This is almost 24% larger width compared to baseline current of 100 A, indicating that width is directly proportional to the current. The pulse and short/spray modes reduced the width by 2.65 mm and 4.72 mm, respectively. All these results are statistically significant, with *P* values lower than 5%. Furthermore, the interactions between modes and current are also significant, suggesting that the combined higher currents and specific modes can

Table 4 Summary of regression analysis for input variables at various levels relative to the baseline current (100 A) and baseline mode (D. Pulse) against each response variable

Responses	Input variables	Coefficient	Std. error	*P* value	95% Confidence interval
Penetration	Intercept	1.2217	0.446	0.013	[0.285, 2.159]
	Current (200A)	0.8357	0.631	0.202	[−0.489, 2.161]
	Current (300A)	3.3403	0.631	< 0.001	[2.015, 4.665]
	Mode (Pulse)	−0.4753	0.631	0.461	[−1.800, 0.850]
	Mode (Short)	−0.6701	0.631	0.302	[−1.995, 0.655]
Width	Intercept	7.598	0.742	< 0.001	[6.038, 9.158]
	Current (200A)	0.061	1.05	0.954	[−2.145, 2.267]
	Current (300A)	2.4237	1.05	0.033	[0.218, 4.630]
	Mode (Pulse)	−2.6583	1.05	0.021	[−4.864, −0.452]
	Mode (Short)	−4.7203	1.05	< 0.001	[−6.926, −2.514]
Height	Intercept	1.554	0.46	0.003	[0.588, 2.520]
	Current (200A)	0.6377	0.65	0.34	[−0.729, 2.004]
	Current (300A)	0.946	0.65	0.163	[−0.420, 2.312]
	Mode (Pulse)	−0.211	0.65	0.749	[−1.577, 1.155]
	Mode (Short)	−0.1377	0.65	0.835	[−1.504, 1.229]
Hardness	Intercept	201	9.514	< 0.001	[181.01, 220.98]
	Current (200A)	−7	13.455	0.609	[−35.26, 21.26]
	Current (300A)	−22.6667	13.455	0.109	[−50.93, 5.60]
	Mode (Pulse)	25.6667	13.455	0.073	[−2.60, 53.93]
	Mode (Short)	63.3333	13.455	< 0.001	[35.06, 91.60]

Table 5 Summary of regression analysis for the interactions of input variables at various levels relative to the baseline current (100 A) and baseline mode (D. Pulse) against each response variable

Responses	Interactions	Coefficient	Std. error	*P* value	95% Confidence interval
Penetration	Intercept	1.221	0.446	0.013	[0.285, 2.159]
	Current (200A) × Mode (Pulse)	0.617	0.892	0.498	[−1.257, 2.491]
	Current (300A) × Mode (Pulse)	0.715	0.892	0.433	[−1.158, 2.590]
	Current (200A) × Mode (Short)	0.012	0.892	0.989	[−1.861, 1.886]
	Current (300A) × Mode (Short)	−1.124	0.892	0.224	[−2.998, 0.750]
Width	Intercept	7.598	0.742	< 0.001	[6.038, 9.158]
	Current (200A) × Mode (Pulse)	3.129	1.485	0.049	[0.010, 6.249]
	Current (300A) × Mode (Pulse)	2.059	1.485	0.182	[−1.060, 5.179]
	Current (200A) × Mode (Short)	5.820	1.485	0.001	[2.701, 8.940]
	Current (300A) × Mode (Short)	3.536	1.485	0.028	[0.417, 6.656]
Height	Intercept	1.554	0.46	0.003	[0.588, 2.520]
	Current (200A) × Mode (Pulse)	−0.171	0.92	0.855	[−2.103, 1.761]
	Current (300A) × Mode (Pulse)	0.207	0.92	0.824	[−1.725, 2.139]
	Current (200A) × Mode (Short)	0.539	0.92	0.565	[−1.393, 2.471]
	Current (300A) × Mode (Short)	−0.974	0.92	0.304	[−2.906, 0.958]
Hardness	Intercept	201	9.514	< 0.001	[181.01, 220.98]
	Current (200A) × Mode (Pulse)	−21.666	19.028	0.27	[−61.64, 18.31]
	Current (300A) × Mode (Pulse)	−22.333	19.028	0.256	[−62.31, 17.64]
	Current (200A) × Mode (Short)	−67	19.028	0.002	[−106.97, −27.02]
	Current (300A) × Mode (Short)	−52	19.028	0.014	[−91.97, −12.02]

substantially influence the bead width in the WAAM process. For example, at 200 A, the width increased by 3.12 mm in pulse mode and by 5.82 mm in short/spray mode, whereas at 300 A the width increased by 3.53 mm in short/spray mode with respect to baseline value of width. The regression results for height conform to the results of height obtained from ANOVA analysis, showing no significance for input variables and their interactions. In addition, we obtained 201 HV for hardness at baseline, i.e., at 100 A and double pulse mode. This was significantly increased in short/spray mode by 63 HV with a *P* value of less than 0.001. Besides, significant interaction between the short/spray mode and current were observed. At 200 A the hardness decreased by 67 HV and at 300 A it decreased by 52 HV, respectively. This reveals that the short/spray mode generally increases the hardness compared to pulse and double pulse transfer modes; however, this is mitigated at higher current levels.

Following the statistical significance of interactions between current and transfer mode for bead width and hardness from ANOVA and regression analysis, the interaction plots were obtained for these significant response variables which are shown in Fig. 4. The non-parallel lines reveal that an interaction exists between the independent variables against the dependent variables at various factor levels. Focusing on the bead width, the short/spray transfer mode represents a sharp increase from 100 to 200 A; however, it diminishes beyond 200A but stays within the values obtained for 200A. On the other hand, pulse transfer mode at 100A starts at an intermediate width with respect to the other two transfer modes and exhibits a more gradual increase with higher currents.

Moreover, double pulse transfer mode starts with a higher width at 100A with a negligible increase at 200A and further increases to the highest with respect to other transfer modes at 300A. However, the important thing to notice is the range within which the value of width lies for a certain current and transfer mode. For example, at 100 A the mean width differs significantly in different transfer modes but at higher current values, i.e., 200 and 300 A, mean width falls within a range not so different in three transfer modes, nevertheless, a distinction exists between them.

The interaction plot for hardness shows the highest hardness in short/spray mode at 100A which significantly decreases for increasing current levels and remains relatively stable between 200 and 300 A. One possible explanation for this trend could be attributed to the transition between the short-circuit transfer mode to spray mode at higher current levels where the spray mode incorporates a higher heat input as compared to short-circuit mode and ultimately changing the material characteristics. Pulse transfer mode starts with a moderate hardness at 100 A, while double pulse yields the lowest hardness at the same current of 100 A. Similarly, pulse and double pulse modes show a more uniform decrease when increasing the current to 200 and 300 A, respectively. Furthermore, at 200 and 300 A all the transfer modes show a difference of ± 10–15 HV.

In addition, the interaction of input variables, i.e., current and transfer modes, did not show statistical significance for

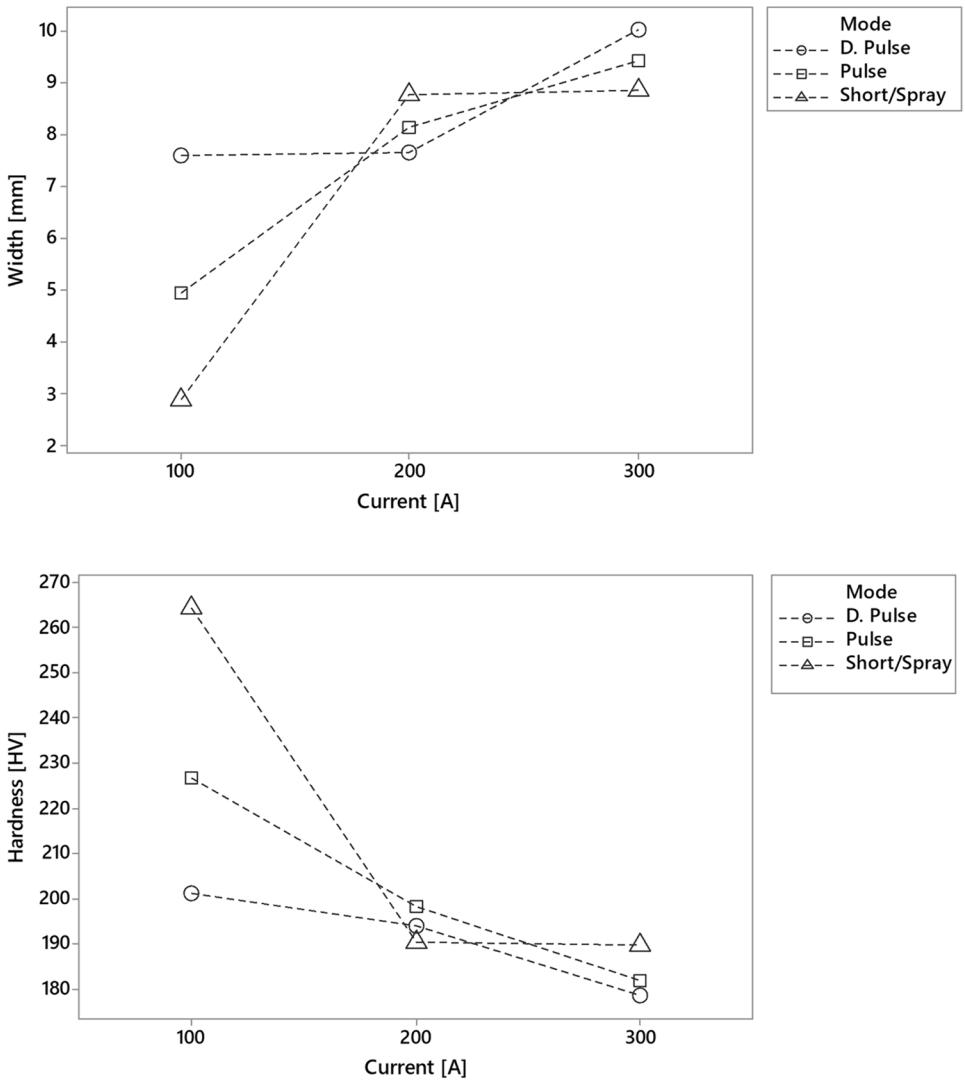

Fig. 4 Interaction plot of statistically significant interactions

bead penetration and height from ANOVA and regression analysis. To verify these results graphically, the interaction plots for height and penetration are shown in Fig. 5. An increasing upward trend for penetration is evident from 100 to 300 A, indicating a direct relationship between the current and bead penetration. However, the lines representing each mode remains substantially parallel, representing non-significant interactions. Thus, irrespective of the metal transfer mode, the current yields similar penetration depth at a certain level; however, an increased current results in higher penetration. Similarly, looking at the interaction plot of height, one can observe an increasing trend in general. Nevertheless, this trend vanishes tremendously when the current is increased from 200 to 300 A in short/spray transfer mode. For each deposit, the samples were cut at three distinctive locations: at the start, in the middle and at the end of each bead, and their values were averaged for each response variable. In WAAM deposits, typically the bead height tends to reduce at the last section of the bead compared to the rest of the deposit. We observed a severe height reduction at 300 A at the last section of the bead, reducing the average height significantly. This could be attributed to the fact that during the sample preparation, the third sample of the bead, deposited under 300 A in short/spray mode, was cut much closer to the cross section with reduced height. We assume this phenomenon has resulted in the statistical non-significance of height. However, in practice we expect a positive relationship between the current and height [40] which is also reflected in the pulse and double pulse transfer modes, as well as from 100 to 200 A in the short/spray mode in our study.

The scatter plots of actual data with predicted regression lines are shown in Fig. 6. The shaded areas around the regression lines indicate the certainty of the estimated relationships with a 95% confidence interval. A narrower area, closer to regression lines suggests a higher precision of the estimated relationships. The graph further supports the obtained results and interpretations. For example, the

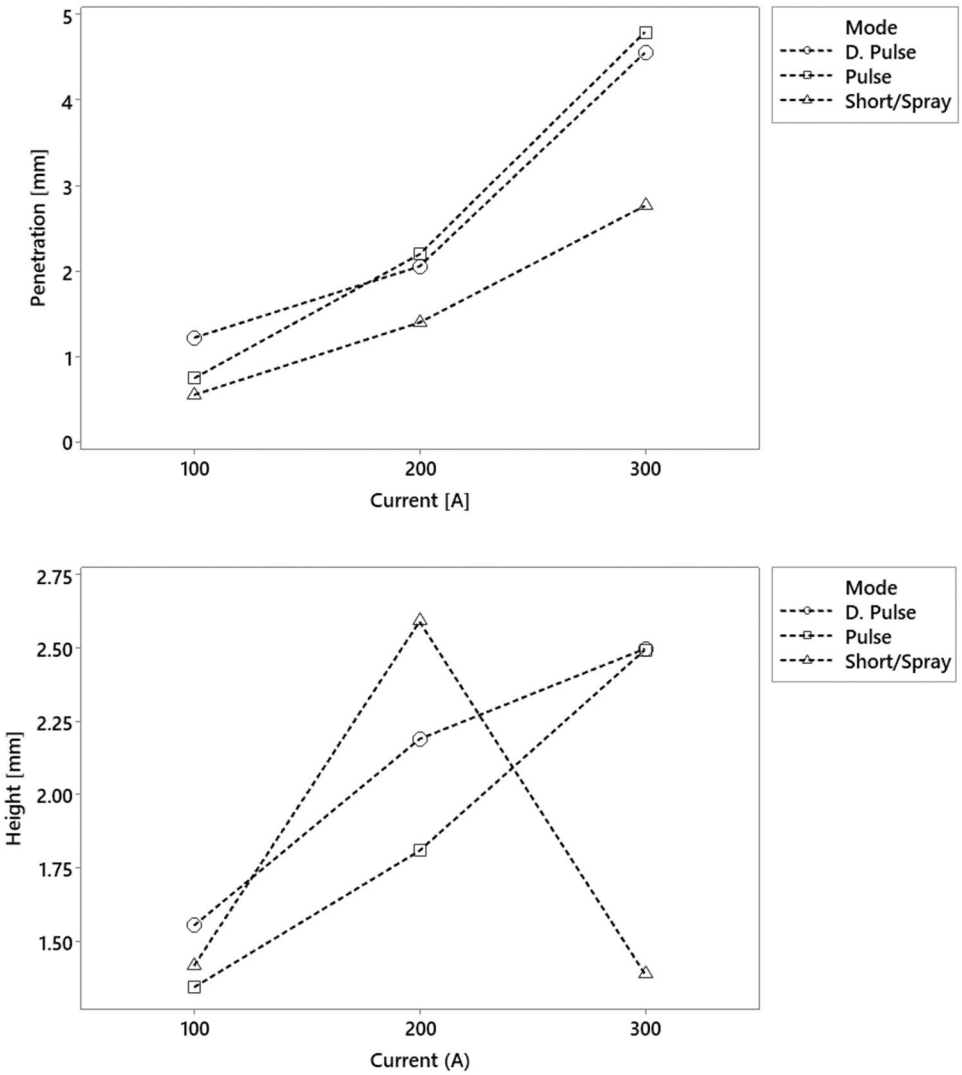

Fig. 5 Interaction plot for statistically non-significant interactions

graph represents a positive and consistently increasing trend between the current and penetration. The highest penetration for each mode can be observed at 300 A. At 100 and 200 A, the penetration depth does not deviate significantly across different modes. Similarly, the width shows a rising trend with increased current which is more evident in case of pulse and short/spray modes, showing a more robust relationship between the current and width across these transfer modes. As seen before, height represents high variability which is represented by larger shaded area around the regression lines. The highest height is shown at 200 A in short/spray mode with huge variability of data, while other modes show less fluctuations. The graph shows a relatively more evident decreasing trend in pulse and short/spray modes as the current is increased; however, double pulse demonstrates a more stable trend at various current levels. The highest current is observed in short/spray mode at lowest current level.

Figure 7 represents the results of shape characteristics for bead-on-plate deposits, including the penetration, width, and height. Deposition current at different levels exhibits considerable effects on dependent variables. Similarly, the metal transfer mode also plays a vital role. In fact, changing the deposition current changes the penetration and width but also the mean values are varied with different transfer modes used in this study. The global trend for these values increased for all metal transfer modes when the deposition current was increased from 100 to 200 and then further to 300 A except for height where the increasing trend diminishes between 200 and 300 A. This could be the reason for the statistical insignificance of height in ANOVA analysis. WAAM is a complex process and sometimes the arc instability causes inconsistency in bead characteristics of deposited beads which might be the case here. However, an increasing trend is expected for the height as the current increases from 200 to 300 A. Furthermore, for the same current levels, the transfer modes play their respective role for the response variables under study. For instance, at 100 A current the penetration slightly increased from short-circuit to pulse mode

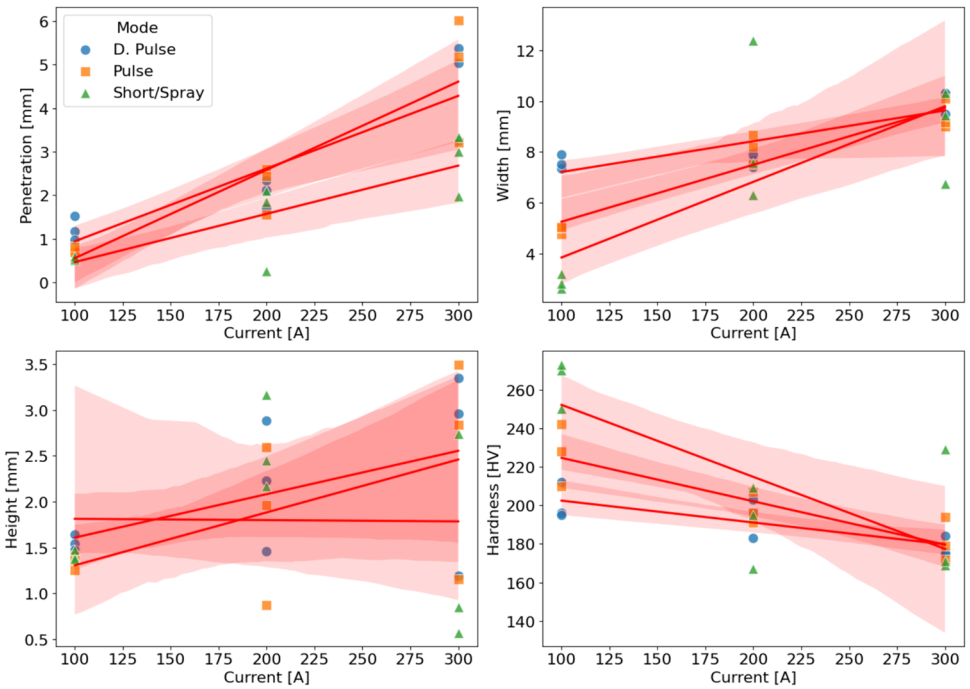

Fig. 6 Scatterplot of response variables with regression lines against the input variables

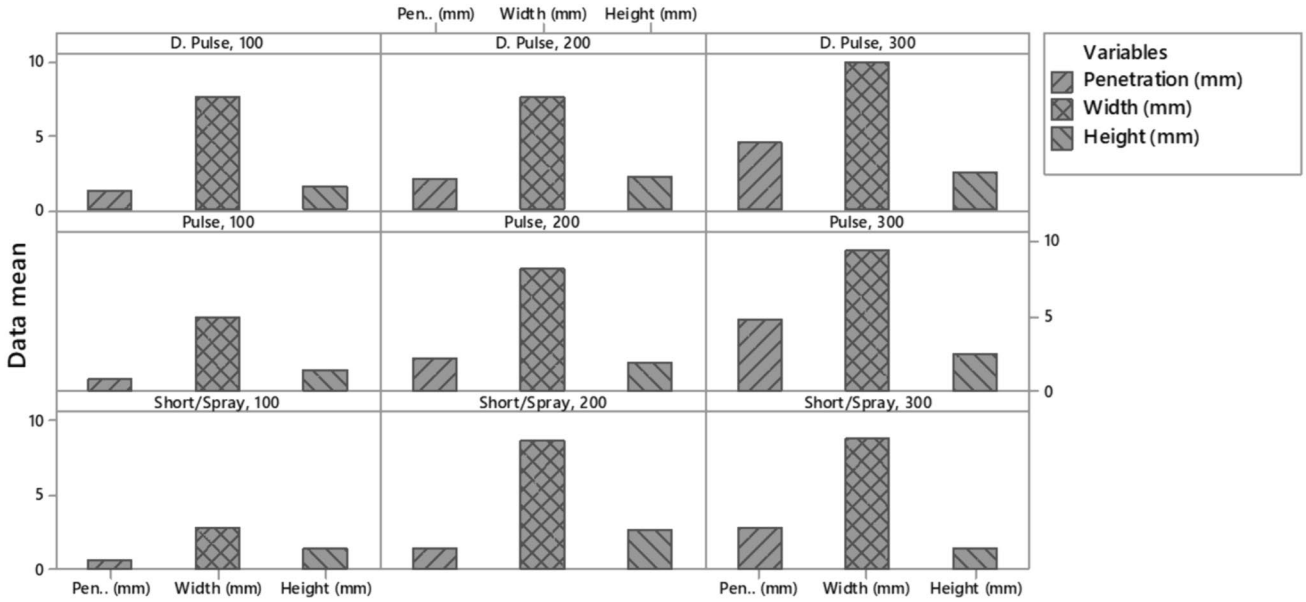

Fig. 7 Chart of means of bead characteristics against deposition current and metal transfer modes

and then further to double pulse mode. The same phenomenon can be observed for width and height.

Figure 8 contains the main effects plots, showing a conclusive overview of the main effects of independent variables for each response variable without considering their interactions. In short, the "Mode" column takes the average of the response variable for each mode, irrespective of the current level and plots them. Similarly, the "Current (A)" column takes the average of the response variable at a certain current level irrespective of the transfer mode. This gives a clear understanding of the effects of current and transfer mode individually. For instance, width is linearly increasing between the current levels but at the same time we can observe a declining trend between the metal transfer modes. The highest width value was recorded in double pulse transfer mode and short/spray mode resulted in the

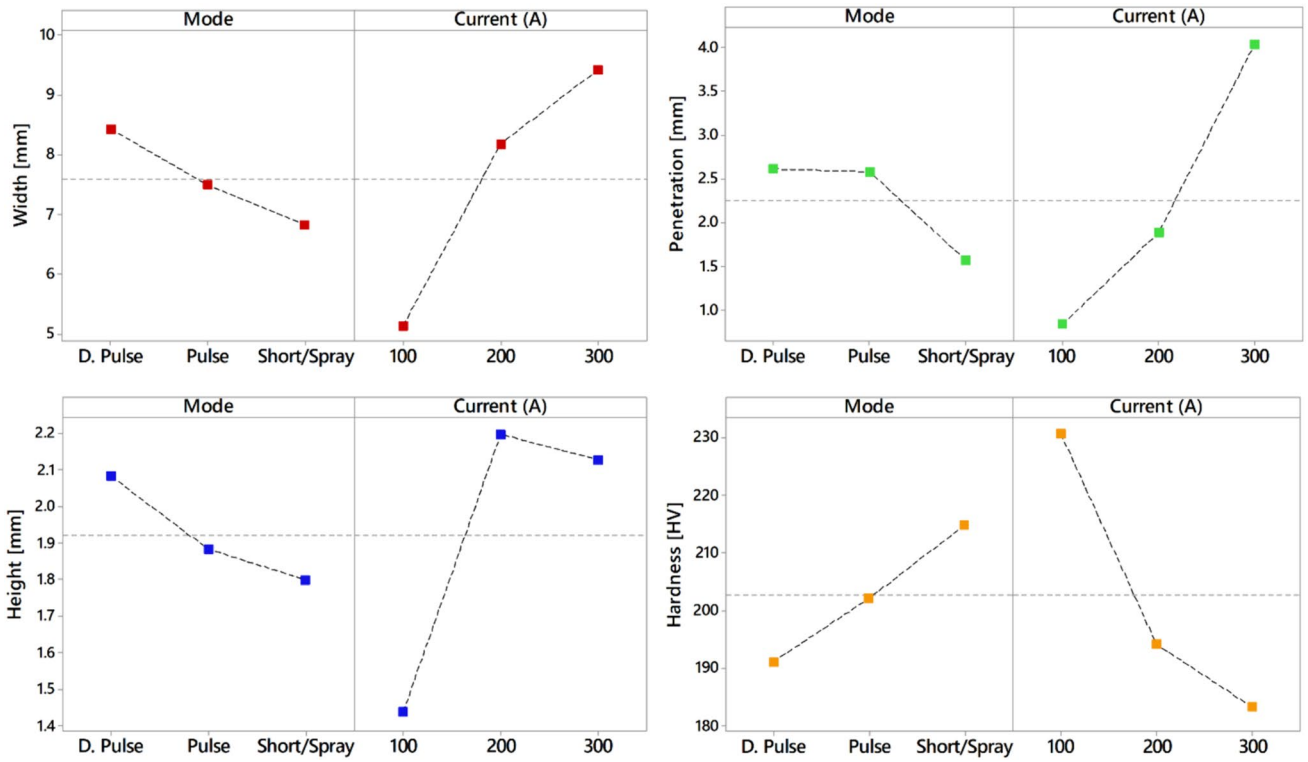

Fig. 8 Main effects plot of width, penetration, hardness, and height for deposition current and transfer mode

lowest, while pulse mode showed intermediate width. A similar trend can be seen for height with the only exception that a decline is observed between 200 and 300 A which was discussed earlier. Moreover, a deeper penetration is observed with increasing level of deposition current, while a decreasing trend is seen across transfer modes but pulse, and double pulse modes show similar penetration range, while short/spray mode contributed for the lowest. Finally, hardness decreases continuously with the increase of current level where short/spray transfer mode resulted in highest hardness, while double pulse produced the least hard samples.

WAAM process is still premature, and there is no universally common heat source; control parameters differing across various WAAM systems. Some older WAAM power sources allow the selection of the main input variables individually. These variables on the heat source include the deposition current, voltage and wire feed speed (WFS). The advancement in heat sources with improved electronics introduced the synergic control heat sources where only one of these variables is set on the controller, and the other two input variables are automatically adjusted according to a synergic curve. This curve is based on factors such as the chosen metal transfer mode, wire material and diameter, and the selection of shielding gas and its composition. Moreover, these input variables are usually proportional to each other, meaning that any increase in one variable would lead to a corresponding rise of the others.

However, considering the effects of these input variables on bead morphology, we observe similar trends when comparing the existing results from various researchers in the literature. In a relevant study [41], Taguchi technique, analysis of variance (ANOVA), regression modelling, and gray relational analysis (GRA) were used to investigate the bead morphology with respect to wire feed speed, deposition speed, and voltage. They found that wire feed speed proportionally increased the bead height, bead width and penetration depth. That makes sense, because increasing the wire feed speed increases the amount of material deposited from the filler wire. This in turn, causes a rise in current and voltage in the heat source. If the deposition speed is kept constant, any increase in current and voltage rises the heat input, subsequently increasing the bead width and penetration. The literature further revealed in another study [42] that bead width increases with the increase of wire feed speed and voltage within specified ranges of 5–8 m/min and 18–24 V, respectively. This is because the higher voltage leads to an expansion and spread of electric arc, creating larger beads. However, bead height exhibited variations where an elevated wire feed speed increased the deposition of material per unit length, contributing to higher bead height. Conversely, voltage and deposition speed ranging from 18 to 24 V and 0.3

to 0.6 m/min reduced the bead height. As mentioned above, higher voltage results in a larger arc spread and increased amplitude, leading to increased heat input. This results in a flatter bead and reduced bead height. A.L.B. Novelino et al. [43] also found similar relationships for bead morphology by investigating the deposition parameters on bead geometry with a cold metal transfer (CMT) power source. The study revealed an explicit correlation of input variables with bead morphology where increasing the wire feed speed, current and voltage resulted in an increase of bead width and height.

In our study we used a synergic control heat source where the wire feed speed is directly proportional to the deposition current. Hence, we can relate the observed trends from the literature with our study where we found that a positive proportionality existed between the current and the bead shapes; however, considering the interactions between the current and various transfer modes, a more complex phenomenon establishes, needing proper tuning and trials of the input variables based on specific bead characteristic requirements.

A detailed analysis of the hardness profiles of the bead-on-plate deposits was carried out from top to bottom in each sample which are reported in Fig. 9. Metal transfer modes and deposition current were explored while keeping the deposition speed constant at 11 mm/s. The Vicker's hardness indentations were started at the top edge of the single beads leaving a 0.5 mm tolerance from the top edge and extending across the middle zone, HAZ and base metal for all beads. A distinctive variability was realized for hardness in short circuit, pulse, and double pulse transfer modes at the three levels of deposition current. This is understandable, since various transfer modes and current levels can incorporate varied heat inputs and ultimately result in dissimilar hardness values. In our study, the highest hardness values were found for short-circuit transfer mode and increasing the deposition current resulted in lower values of hardness in all transfer modes. Hardness decreases from the top of the single beads towards the base metal, and this is more evident especially at lower and intermediate current levels. Similar results were observed for hardness in another study [44] with AISI 410 steel. The peak hardness value was observed in the upper edge of the samples deposited with short-circuit transfer mode at the deposition current of 100 A; however, the short-circuit mode produced more spatter during the deposition.

The variability of hardness profiles across various metal transfer modes and current levels results from arc behavior, melt-pool dynamics and relevant cooling rates. The higher hardness profile near the top of the bead at lower currents can be attributed to faster solidification and lower heat input, leading to finer microstructure. For example, in short/spray mode, lowest current level produced a smaller melt-pool and a corresponding smaller bead size. Considering its size and the cold substrate, this might have experienced very

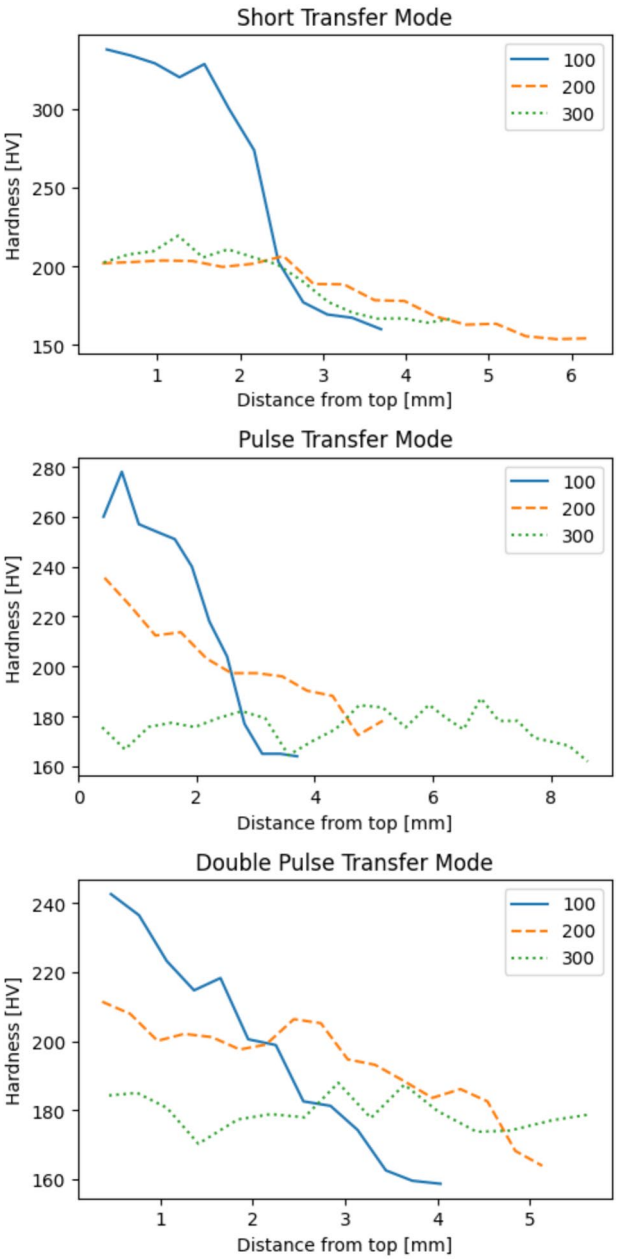

Fig. 9 Hardness vs deposition current in different metal transfer modes

fast cooling during solidification. The faster cooling normally results in finer microstructure, subsequently leading to higher hardness. However, with higher current, the wire feed speed increases. That means a larger melt-pool and higher heat input. As a result, the solidification becomes slower and causing the annealing effect and grain coarsening, which causes a lower hardness. Moreover, short-circuiting transfer mode typically operates at a lower voltage and higher actual current compared to the nominal current supplied to the heat source. Consequently, creating a more turbulent arc,

causing a localized higher heating and corresponding rapid cooling. The frequent contact between the electrode and the workpiece further contributes to this phenomenon, making an unstable melt-pool.

On the other hand, pulse transfer mode exhibits hardness profiles that reflect a more consistent heat input and controlled cooling rates. This is attributed to the pulsed nature of the arc that helps in achieving a more stable melt-pool and better heat distribution. Similarly, for double pulse mode, the hardness profiles suggest severe thermal cycle effects due to alternating high and low current pulses, promoting refinement of microstructure at lower current level. However, at higher current levels the hardness reduces due to prolonged exposure to high temperatures.

It is important to note that at lower current, the hardness profiles in all transfer modes start at a high peak hardness at the top of the beads; however, it undergoes a sharp reduction from top to bottom. Such a hardness profile has been reported in the literature [45] for a bead-on-plate deposit. However, as the deposition current increases, instead of a steep curve, the hardness profile shows a gradual decrease from top to bottom. This indicates slower cooling at higher currents, resulting in a coarser microstructure that reduces the hardness. Nonetheless, such a profile reflects a more homogenous grain structure from top to bottom of the deposited beads.

Figure 10 represents the optical microscopic images for the microstructure of bead-on-plate depositions. At low level current, all metal transfer modes show a fine and lamellar microstructure due to low heat input and corresponding faster cooling with cold substrate. The microstructure then tends to form polygonal and columnar grains or a compromise between them when the current is increased to 200 and further to 300 A. In case of short/spray transfer mode, the microstructure shows a lamellar appearance and finer microstructure in the matrix when the deposition current is 100 A. In the sample where the deposition current was increased to 200 A, a similar microstructure that was seen for 100 A except that grain coarsening is evident and interlamellar spacing became larger; led to less densely scattered lamellae within the ferrite matrix. Polygonal ferrite grains appear at 300 A and show some pearlite islands at grain boundaries. In this case explicit grain coarsening is observed. Moreover, in pulse transfer mode at 100 A, randomly oriented cementite plates with slightly longer lamellae are present as compared to short/spray transfer mode. Substantial grain coarsening is observed at 200 and 300 A and some small pearlite islands can be seen at grain boundaries at 300 A. Furthermore, a polygonal grain structure is observed at 300 A, while a partly columnar grain structure appeared at 200 A. Similarly, at low current in double pulse mode, a finer microstructure is produced at low current level which is not

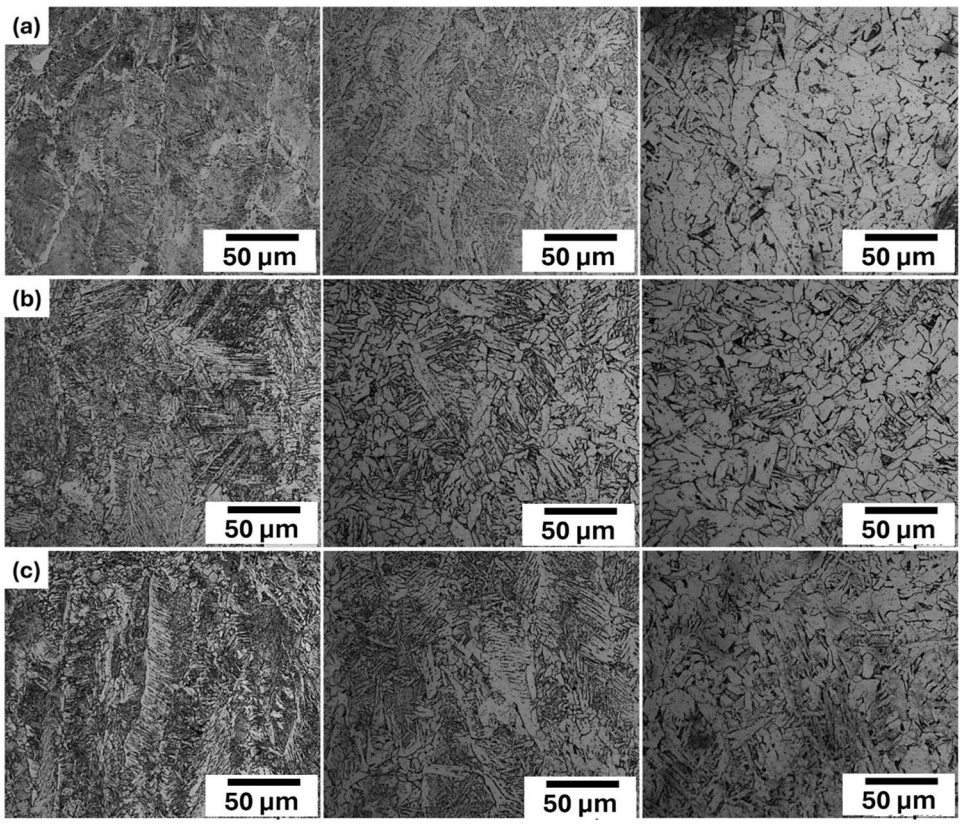

Fig. 10 Optical microscopic images of the fusion zone for 100, 200 and 300A current from left to right, respectively: **a** short/spray mode, **b** pulse mode, **c** double pulse mode

significantly different from pulse mode. However, a coarse columnar microstructure can be observed at 200 A where grain coarsening increased further when the deposition current was increased to 300 A. In all metal transfer modes, the increasing deposition current increased the volume fraction of ferrite phases and probably leading to a softer material which was observed in the microhardness.

Research [46] shows that thermal gradient and lower cooling rates, which are both influenced by higher currents, result in grain growth in fusion-based additive manufacturing processes. Similarly, it was shown that the percentage of smaller grains increased as the current was raised from 120 to 170 A, keeping the voltage and deposition speed constant [47]. In summary, the tendency of the microstructure to show marginally enlarged grain size as the deposition current increased suggests a direct correlation between current level and corresponding heat input and solidification rate. This relationship indicates that the microstructure of the deposited material can be tailored by carefully controlling the deposition parameters, particularly the current levels for a certain metal transfer mode. A sophisticated approach is necessary to optimize deposition settings for specific applications, as such a control offers important implications for achieving desired material properties.

Furthermore, Fig. 11 reports the dilution, which offers important insights into the re-melting regions of substrate (or previously deposited layers) in WAAM under various metal transfer modes and current levels. Dilution resulting from short/spray, pulse, and double pulse transfer modes at different current levels is investigated, and the results shed light on the intricate dynamics of WAAM process. As the current level rises, the short/spray transfer mode results in a noticeable increase in dilution. At 100 A, a 27% dilution suggests a somewhat regulated fusion-to-penetration ratio. On the other hand, dilution increases to 31% and 66%, respectively, as the current increases to 200 and 300 A, respectively. The dilution profile of the pulse transfer mode is different from that of the short/spray transfer mode. At 100, 200, and 300 A, the dilution percentages are 46%, 47%, and 55%, respectively. These comparatively constant dilution levels at different currents imply a more stable fusion-to-penetration ratio in the pulse transfer mode. The controlled pulsing of arc in pulse transfer mode could lead to a more even distribution of energy, which in turn affects the interaction between the penetration and fusion areas. This can be useful where preserving a constant dilution is necessary to obtain a specific outcome. The dilution percentages in the double pulse transfer mode exhibit a pattern that is comparable to that of the pulse transfer mode, but with comparatively smaller values. The dilution is 41% at 100 and 200 A. Nevertheless, the dilution rises to 56% at 300 A. This implies that the double pulse transfer mode provides somewhat consistent and controlled dilution levels, just like the pulse transfer mode.

3.2 Multi-track deposits

Wire arc additive manufacturing process has the potential for depositing large parts which are based on single beads deposited side by side or overlapped with a certain hatch distance and then layered in the build direction. It is crucial to select the right parameters to obtain a structurally sound part with desired geometry. Figure 12 represents the as-deposited samples and the cross sections from macroscopic images, showing the bead morphology of multi-track deposits. The deposition was conducted with different hatch distance and deposition current without stacking but partially overlapping the layers to study the combined effects of current and hatch distance. From top to bottom, 80, 120 and 160 A currents were used and for each current level from left to right a hatch distance of 2, 3, and 4 mm were used, respectively.

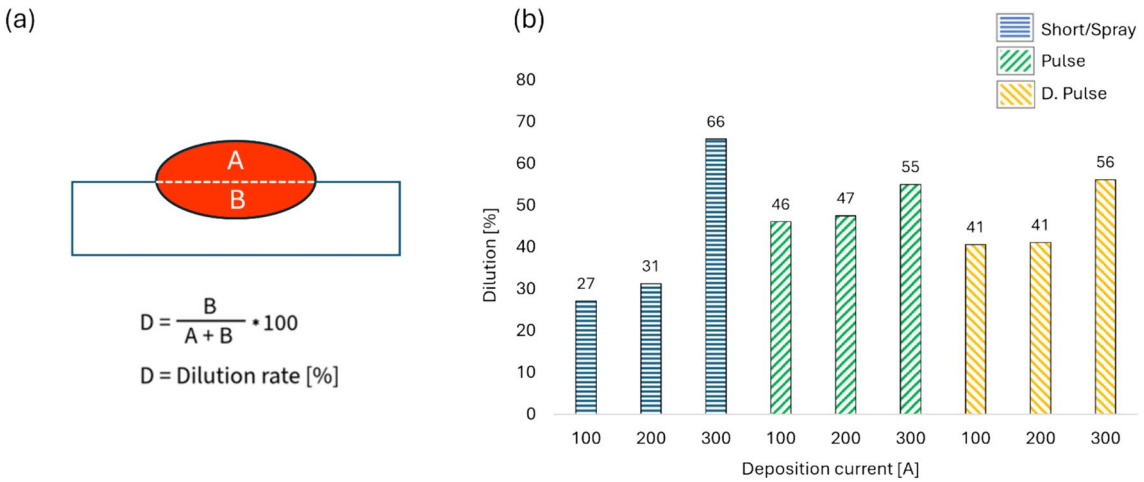

Fig. 11 Showing **a** schematic for dilution measurement, **b** dilution for bead-on-plate depositions under each transfer mode at three current levels

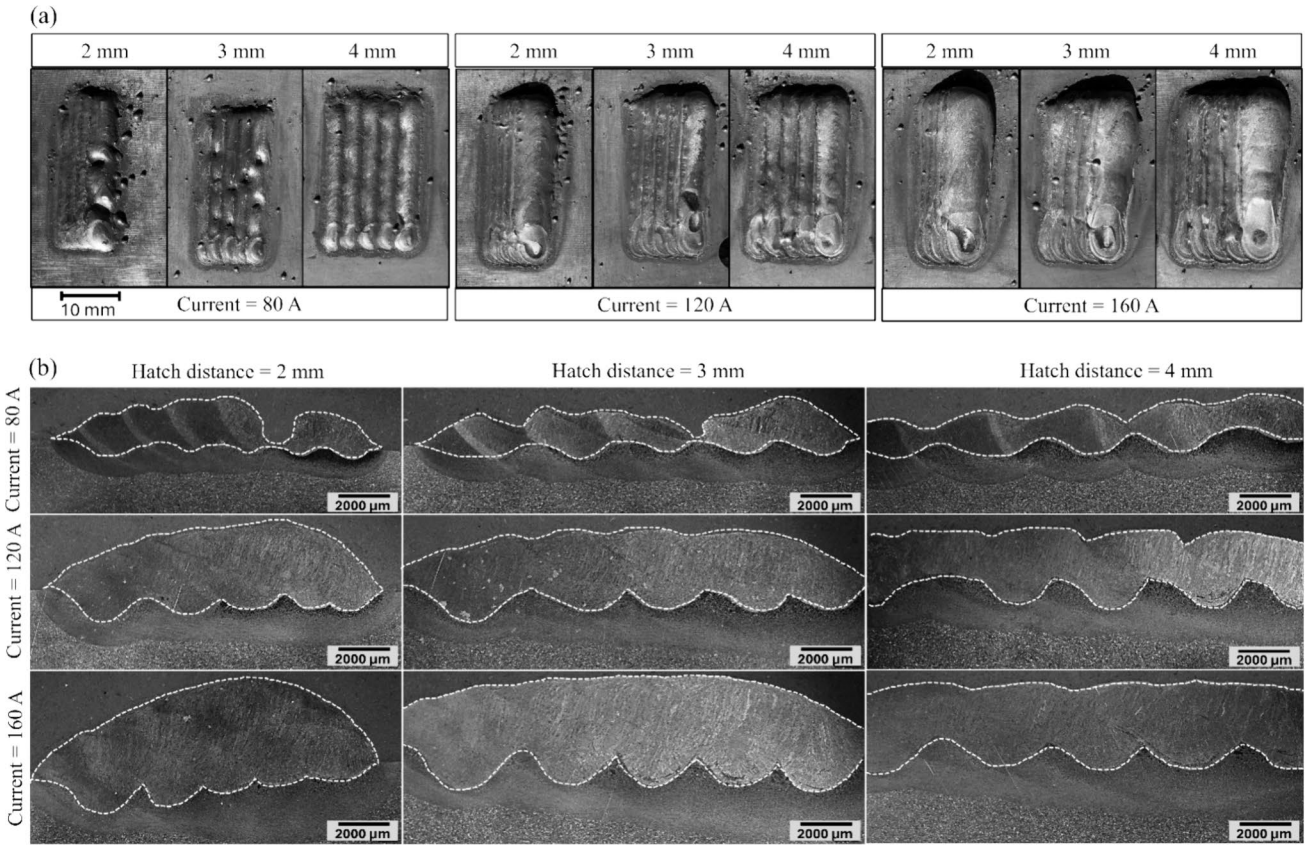

Fig. 12 Multi-track deposits with various combinations of current and hatch distance: **a** as-deposited samples, **b** macroscopic images of cross sections

From the macroscopic images, an evident effect of deposition current and hatch distance is observed. It is shown that the ratio of the height between the first and the adjacent bead depends on proper overlapping or hatch distance [48]. More specifically, a low current level combined with high hatch distances results in valleys between the adjacent beads. Conversely, higher current combined with low hatch distances leads to elliptical shapes instead of flat surfaces. A lower hatch distance decreases the cooling rate during solidification by increasing the overlapping and melt-pool size [49].

Moreover, the shape of the individual bead penetration also modified depending on various combinations of current and hatch distance. For instance, at 80 A current and higher hatch distances of 3 and 4 mm, valleys are formed and significant unevenness on the surface takes place. This happens due to a lower wire feed speed corresponding to the low current level, resulting in insufficient material deposition. This further exacerbates when the hatch distance is increased and filling the material too thinly, failing to completely cover the gaps between the adjacent beads. Such geometrical inhomogeneity and irregularity not only influence the geometry of the product [50] but also effects the microstructure and induced welding defects [51].

Increasing the current to 120 A and 160 A, the valleys between the beads become less pronounced. The higher current increases the wire feed speed and more material deposited, leading to comparatively smoother surfaces. The higher current also increases the heat input that improves the melting and flow of material to effectively fill the gap with more material feed rate. The higher heat input also increases the penetration and the corresponding dilution ratio, which can influence the microstructure and mechanical properties of the deposited structure. Hence, requiring proper tuning of these parameters. For example, higher current levels with low hatch distance produces unwanted material buildup, forming a circular cross section. This phenomenon is particularly evident at a 2 mm hatch distance with 120 and 160 A of current, respectively.

Thus, the interaction between the current and hatch distance is very crucial. At a constant deposition speed, lower current levels minimize the heat input that is normally desirable for microstructural characteristics. However, lower current would result in poor surface quality if not optimized with an appropriately small hatch distance. Conversely, higher current increases material deposition, effectively filling the gaps between the adjacent beads to produce

smoother surfaces. However, proper interactions of current and hatch distance are needed to obtain an acceptable trade-off between surface characteristic requirements, penetration depth, heat input and corresponding mechanical properties. Considering the visual aspects of the deposited multi-track deposits, we observed a comparatively smoother surface at 160A current with a hatch distance of 3 mm.

3.3 Thin wall

The thin wall was deposited in pulse transfer mode, which is desirable for many reasons. It produces a lower heat input at moderate current levels, provides more consistency for penetration depth and dilution, results in lower spatter generation and offers better arc stability. The deposition direction was fixed for all layers, as shown in Fig. 13.

The as-deposited thin wall, its macroscopic cross section and the microstructure along the building direction is shown in Fig. 14. The underlying microstructure shows distinctive morphology across the thin wall. At the top section of the wall the microstructure consists of a mixture of plate-like and randomly oriented nonlamellar cementite lamellae, partially present as embryonic lamellar grouping across the ferrite matrix such that forming a spheroidite microstructure. This is particularly associated to a slower cooling when the cementite lamellae partly break down into irregular morphology. The presence of allotriomorphic ferrite is also evident. As we move in the building direction from top to middle, the microstructure tends to form a predominantly elongated appearance and partially presents coarse ferrite grains. Very small pores can also be seen in the middle of the wall. The presence of defects was also reported by [52]

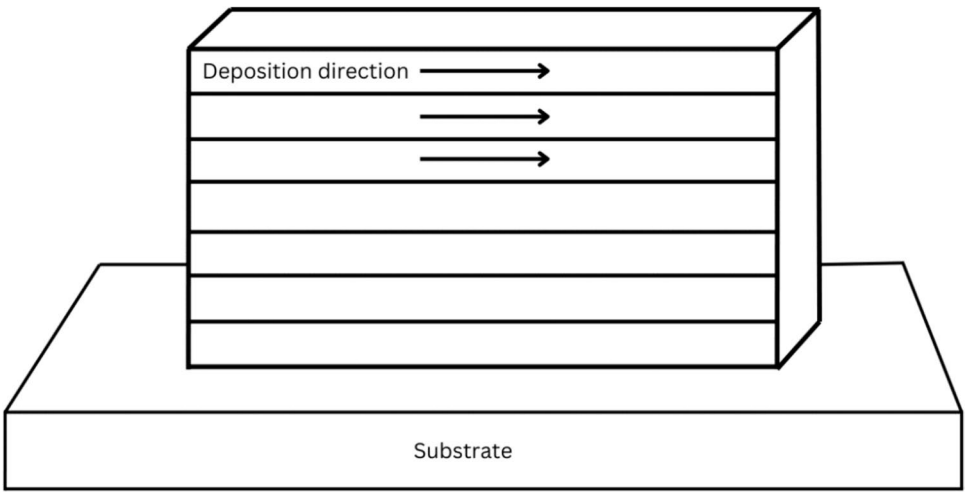

Fig. 13 Deposition strategy used for thin wall

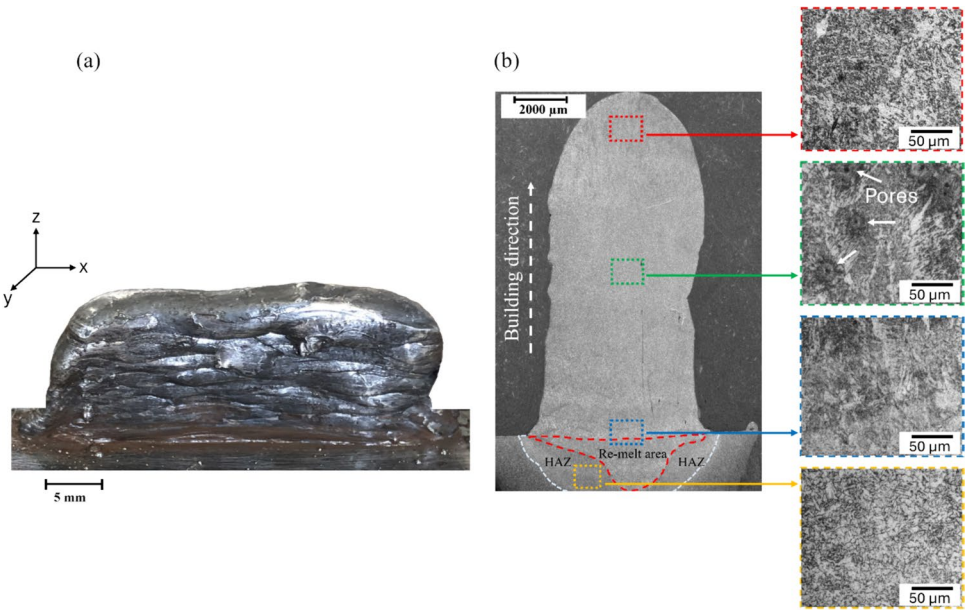

Fig. 14 **a** As-deposited thin wall, **b** macro- and microstructural images at various sections in the building direction

along-with certain impurities and lack of fusion by image analysis where they calculated 0.15% porosity, 0.08% impurities and 0.04% lack of fusion, respectively. Moreover, at the bottom region the transition from fusion zone to re-melt area is shown, revealing a more uniform structure with finer grains. However, the heat effected zone (HAZ) consisted of coarser polygonal and partly columnar grains. The underlying microstructure for thin wall ER70S-6 was also reported in previous studies [53–55].

The observed variations of the microstructure are attributed to the inherent thermal history in the WAAM process. The typical factors influencing the microstructure of a thin wall include the heat input, cooling rate and the thermal cycles. Each of the newly deposited layer experiences a certain heat input associated to the input variables on the heat source and the deposition speed controlled by the motion system. As the number of layers increase in the building direction, a subsequent thermal cycle is experienced by the previously deposited layers. Consequently, the continuous heating and cooling cycles induce a tempering or annealing effect and may lead to grain growth and phase transformation. Furthermore, the associated cooling rates also influence the overall build structure where faster cooling results in finer grains and the formation of martensite and bainite structures. Similarly, a slow cooling during the solidification causes grain coarsening and favors ferrite and pearlite. In short, the microstructure of a material responds based on its composition, build size, thermal history, and deposition parameters. A proper inter-layer delay time could also be beneficial for certain microstructural requirements [56].

Apart from the microscopic study, scanning electron microscopy (SEM) analysis was performed on the thin wall in the building direction, focusing primarily at three distinctive locations, i.e., at bottom, in the middle and at the top sections of the wall. SEM analysis is represented in Fig. 15, further enhanced the understanding of the underlying microstructure, revealing certain details that could not be seen in the microscopic study. A well-defined grain structure with uniform distribution can be seen at the bottom of the wall, as shown in Fig. 15a. The higher magnification of segment "A" in the bottom region as shown in Fig. 15d illustrates the presence of equiaxed polygonal grains. This kind of a microstructure is beneficial for the mechanical properties as they enhance the toughness and ductility of

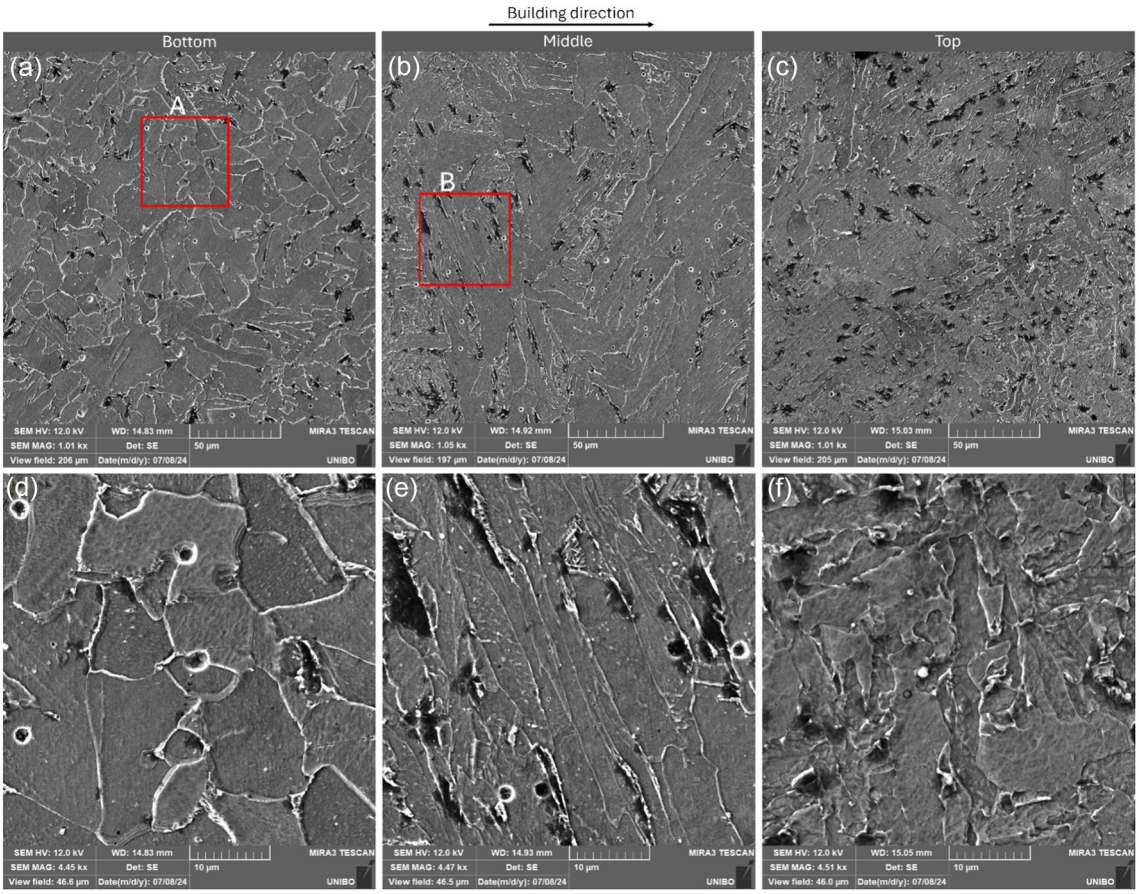

Fig. 15 SEM images of the thin wall along the build direction

the deposited material. Such a microstructure in WAAM process is attributed to a more stable and consistent thermal mechanism due to faster cooling with the substrate during the initial deposited layers. Moreover, very small voids can also be seen along the building direction with varying proportions; representing slightly lower concentration at the bottom compared to the middle and top regions of the wall. Presence of such pores are likely due to continuous deposition in multi-layer structures where contaminations after previously deposited layers are trapped within the melt-pool, potentially leading to such defects [57]. In addition, pores are considered as material-induced or process-induced. Material-induced pores are produced due to contamination of wire or substrate with moisture, grease and certain hydrocarbon compounds that are hard to extract completely, while process-induced pores occur due to poor path planning or unstable deposition and are usually non-spherical [58]. The observed pores across the wall appear to be non-spherical. However, the pore sizes are very small, typically less than 3 microns. Moving to the middle section of the wall, shown in Fig. 15b, the microstructure changes, exhibiting elongated grains. A magnified segment, represented with "B" in the middle part, is shown in Fig. 15e, further detailing the corresponding microstructure. The dark region probably resulted from over etching during the sample preparation. The presence of small porosity is also evident in the middle. Furthermore, an SEM image of the top section is shown in Fig. 15c. A more detailed and magnified segment from the top section is also represented in Fig. 15f. These images present a heterogeneous and coarser morphology compared to the middle and bottom regions. Particularly, equiaxed and elongated grains are dominant, and an evident increase of size is observed in some grains. Such a variation of microstructure is likely due to slower cooling, causing a reduced thermal gradient at the top section of the wall.

Figure 16 shows the microhardness graph of the thin wall representing the hardness profile from the top edge of the wall passing through the middle zone, remelting zone, HAZ until the unaffected substrate has reached. This gives an interesting perspective of the hardness behavior across the deposited wall that ranges between 173 and 263 HV with an average hardness of 203 HV. The highest hardness can be seen on the top edge of the wall which decreases to minimum once reached at the middle of the wall probably due to heat accumulation that corresponds to the microstructural changes, as already shown in Figs. 14 and 15. Then the hardness gradually increases as it approaches the substrate probably because of faster cooling taking place due to conduction heat transfer with colder substrate across the initial layers above the substrate. Moreover, the hardness slightly decreases again when reached in the remelting zone and HAZ due to the thermal cycle experienced during the layer-by-layer process.

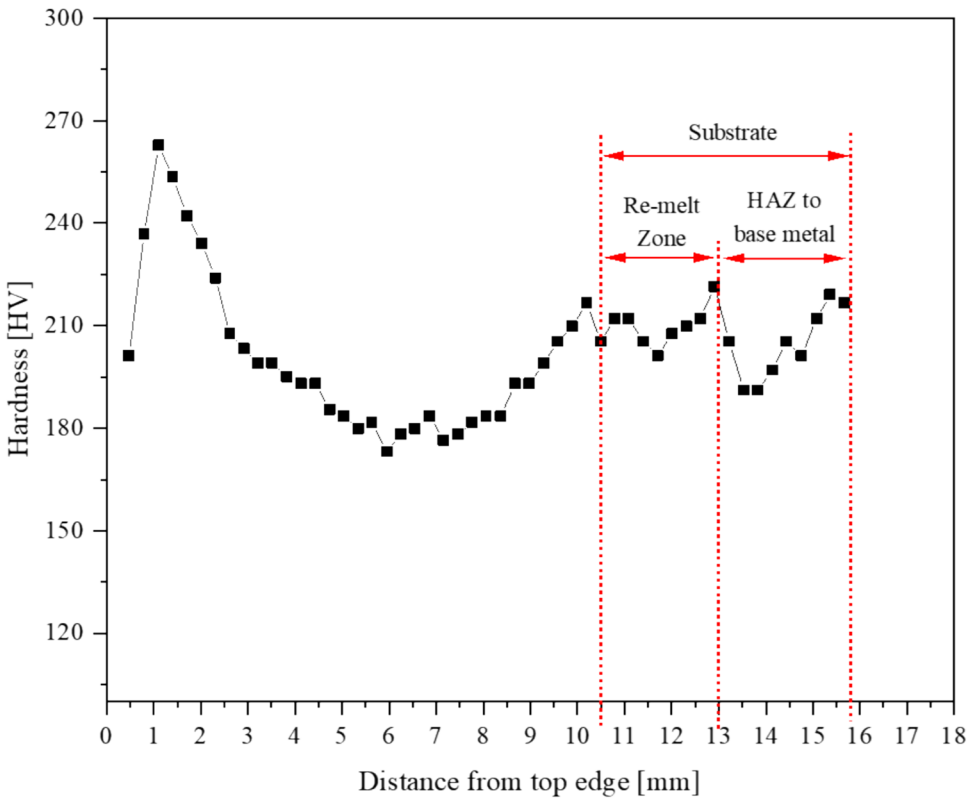

Fig. 16 Hardness profile of the thin wall along the building direction

The three distinct locations in the fusion zone along the building direction experienced different thermal cycles during the deposition and the corresponding microstructural changes took place, resulting in the underlying hardness profile. Interestingly, literature has shown a similar hardness pattern across these specific zones on the wall when depositing an ER70S-6 wire using cold metal transfer (CMT) [59]. Such a hardness profile was attributed to the microstructure and the grain size which slightly reduced from top to bottom. This can be better explained by building a relationship between the number of layers vs heat input, heat input vs grain size, and finally grain size vs material hardness. As the number of layers increase in a multilayer structure, the heat accumulation increases which as a result increases the average grain size due to slower cooling. Therefore, the hardness profile of a thin wall tends to show a reduced hardness at sections where a high thermal cycle and slower cooling rate is experienced.

During the solidification, a significant heat transfer occurs through conduction, passing through the previously deposited layers and dissipated across the substrate. The interface of the substrate in direct contact with the fusion zone undergoes partial remelting. Likewise, the heat effected zone (HAZ) in the substrate also experiences huge thermal shocks in continuous layer wise deposition. Therefore, not only the deposited material but different sections of substrate in closer proximity with fusion area undergo microstructural changes and hence influence the hardness of the material (Fig. 16).

3.4 Cubic structure

A cubic structure was deposited with optimized parameters which are mentioned in materials and methods. The selection of parameters was based on prior trials to produce a defect-free and structurally sound deposition. The deposition strategy for the cubic structure is shown in Fig. 17. The adopted deposition strategy has a higher deposition efficiency for directed energy deposition (DED) process [60].

Figure 18 shows the actual cubic deposit and the microstructural evolution across the deposited block obtained from the optical microscope. As opposed to the thin wall, the microstructure seems to be more homogeneous and comparatively a cleaner microstructure can be seen across the bulk of the cubic structure in the fusion zone. No defects and impurities were found and no proof of lack of fusion were observed from these images. This can be attributed to a more homogeneous heat distribution due to the nature of the build structure with the corresponding scanning strategy. The underlying microstructure is based on lamellar and columnar structure with the presence of allotriomorphic ferrites across the middle and upper sections of deposited cube. Similarly, the microstructure also consists of some acicular ferrites at the upper section. A similar microstructure was reported in a previous study for WAAM structures deposited using an ER70S-6 wire [61, 62]. The microstructure shows a slight increase in the volume fraction of ferrite in the middle section of the cubic structure. As a result, we can assume that the material in that zone could be slightly softer, considering the characteristic properties of ferrite phase. Moreover, the heat effected zone (HAZ) consists of a coarse microstructure with equiaxed ferrites and a few small pearlite islands.

As the solidification proceeds to the center of the overlapping region, it decreases the cooling rate, changing the microstructure to an irregular lath-type morphology [63]. This happens because of more heat accumulation in the central sections of cubic structures, leading to the observed phenomena. We can see such lamellae of lath structure across our samples in the upper and middle sections of the build structure. Employing the same metal transfer mode, i.e., pulse transfer mode and ER70S-6 wire, study has shown a columnar microstructure, exhibiting allotriomorphic and acicular ferrite phases [64]. As the solidification starts from molten material, allotriomorphic ferrites nucleate at the austenite grain boundaries, since these boundaries provide lowest energy barrier. Their nucleation occurs at relatively high temperatures during the initial cooling. Then they grow in thin plate-like structures in an irregular morphology. On the other hand, acicular ferrites usually for at lower temperatures, relating a more complicated nucleation. Their growth is relatively rapid and represents a needle-like shape, forming a finer structure compared to allotriomorphic ferrites. The presence of such a microstructure can be beneficial for structural applications, since they can impart a balance between the strength and toughness of material.

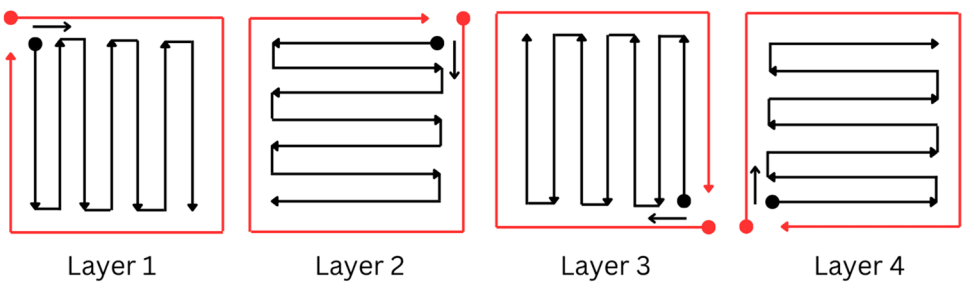

Fig. 17 Scanning strategy used for the deposition of cubic structure

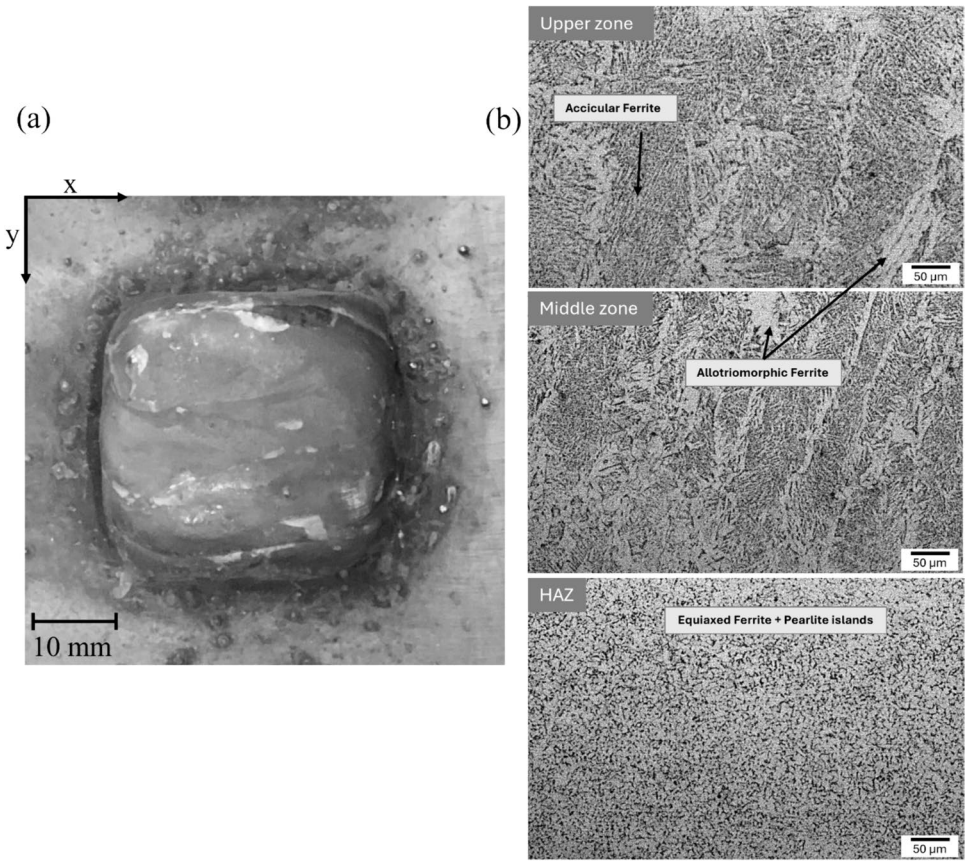

Fig. 18 **a** Actual deposited structure, **b** microstructural evolution at various sections

The SEM images of the cube structure are shown in Fig. 19. The SEM images were obtained from the bottom, middle and upper zones on the structure. For each image, a higher magnification is also provided to exhibit a detailed microstructure. The bottom zone shows relatively finer grains. A comparison of the images with higher magnification reveal that the bottom zone consists of smaller and equiaxed grains with well-defined boundaries across the polygonal grains. The proximity to the cold substrate and the comparatively colder initial layers favors a uniform

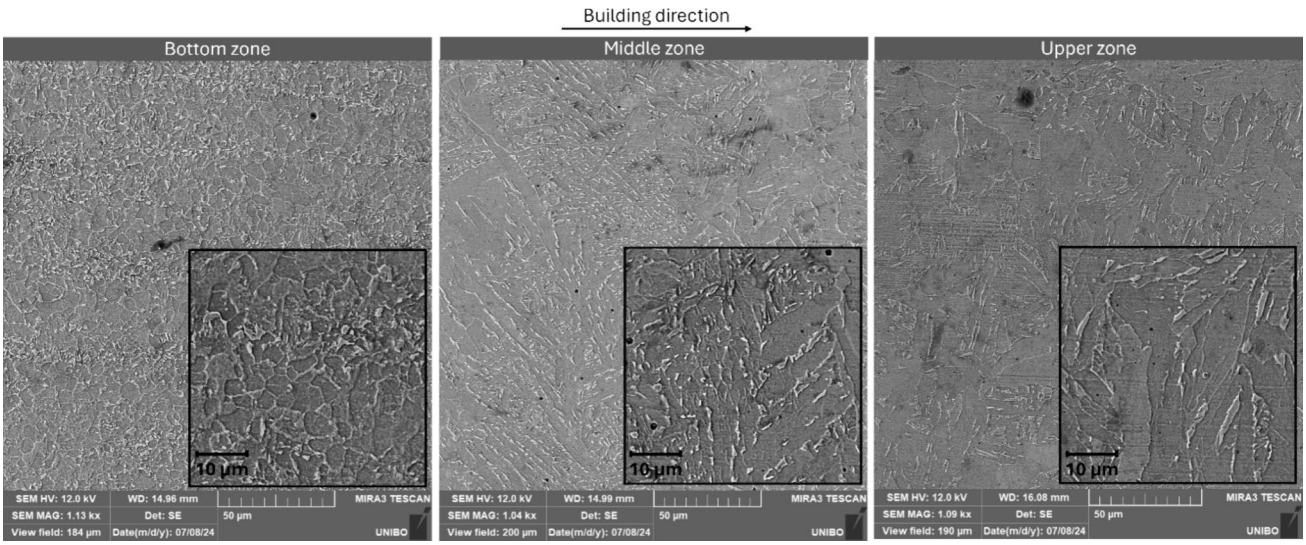

Fig. 19 SEM images of the cubic structure in the building direction

solidification. Hence, it results in a uniform grain growth and finer grains due to faster cooling.

An analysis of the middle zone reveals a significantly different microstructure compared to the bottom zone. The microstructure in the middle zone shows a coarse structure. The elongated and less uniform grain structure is further highlighted in the image with higher magnification. Such a change of microstructure is attributed to the complex WAAM process, experiencing varied thermal cycles in multilayered structures. As the number of layers increase, the WAAM structures experience various thermal gradients at different sections, hence incorporating varied microstructures across the WAAM deposits. Typically, the heat accumulation keeps increasing as we move along the building direction from bottom to upper zones, especially when continuous deposition is carried out in the WAAM process.

Looking at the SEM images of upper zone, we can clearly see a different microstructure. Compared to the middle zone, it shows an even coarser microstructure with larger and elongated grains. The larger and columnar grain structure was also evident in the microscopic images that is an indicative of a slower cooling. The heat transfer in metals primarily occurs through conductive heat transfer. Consequently, less heat dissipation is experienced in the upper zone where a very low thermal gradient exists between the uppermost layers and the lower sections. Since heat is conducted through the previously deposited layers and dissipated from substrate, a lower thermal gradient results in slower cooling at the upper zone which yields a microstructure with elongated and less refined grains. Such a progression in microstructure is typical for larger deposits in the WAAM process.

However, significant wait time between subsequent layers might be necessary if a strictly finer and homogeneous microstructure is needed. In such, a condition, indeed a trade-off between the manufacturing time and microstructural properties, could be possible.

Figure 20 shows the microhardness profile of the cubic structure, starting from the uppermost section of the deposited cube and extending through the middle and bottom, passing through the heat effected zone until reaching the substrate. The hardness moderately decreases from top to bottom with a minimum and maximum hardness of 152 and 210 HV, respectively. An average hardness of 182 HV was calculated from top to bottom. It represents a fairly consistent hardness in the initial segments relative to the top, maintaining the values close to 200 HV. Beyond that, a slight reduction is observed where hardness values drop below 200 HV. As we move further down, small variations are observed; however, the graph remains at around 180 HV. Altought trivial variations can be observed from top to bottom, the overall trend of hardness graph does not show significant variations and aligns well with the underlying microstrucutre. Thus indicating a reasonably uniform hardness from top to bottom with a slight softening in the bottom layers. These small changes are attributed to the microstructural changes and the thermal history during the deposition.

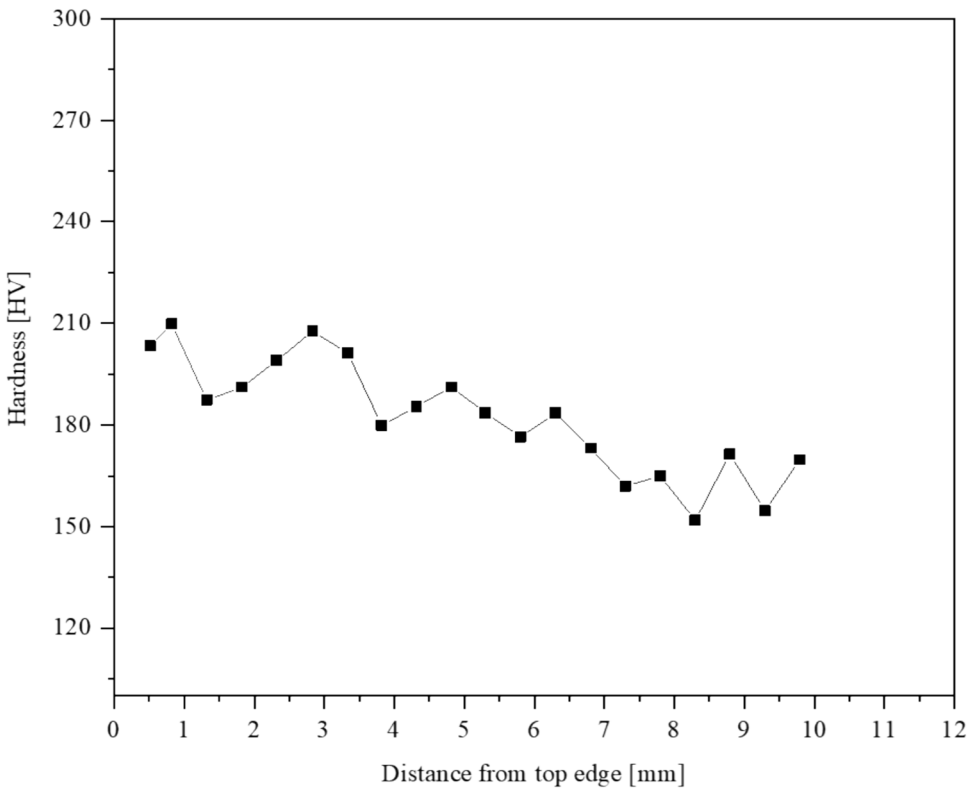

Fig. 20 Microhardness profile of cubic structure

Based on these results, it is safe to assume that the selection of the parameters with the applied depositon strategy results in a homogeneous heat distribution, leading to a fairly uniform hardness profile.

WAAM possesses huge potential for many applications, yet detailed assessments are needed to ensure the long-term durability of WAAM manufactured components. It still lacks quality assurance (QA) standards and methods to guarantee the fitness of WAAM components during operation [59]. However, researchers have investigated the suitability of WAAM components for various engineering applications and compared the properties of deposited components with existing traditional manufacturing technologies. For instance, in such a study it was shown that the average hardness of WAAM deposit was greater, while wear rate was lower than that produced by conventional methods [65]. Reliable methods were used in durability analysis of WAAM products to predict small crack growth which are essential for assessing the long-term durability of additively manufactured parts in critical applications like military aircraft [66, 67]. WAAM fabricated parts can withstand very high cycle fatigue load of 390 MPa up to 2×10^9 cycles [68] which is crucial for long-term durability of WAAM products. However, such benefits are limited for very rough surfaces [69].

Owing to its many benefits, WAAM process finds its applications in various sectors. This includes the successful fabrication of a ship's propeller in Netherlands, called the "WAAMpeller" with the collaboration of a group of companies, including Damen shipyards group, RAMLAB, Promarin, Autodesk and Bureau Veritas [70]. Moreover, WAAM has been employed to print a large-scale stainless-steel bridge [71], in the fabrication of complex fuel nozzles [72], for landing gear assembly and wing spar [73]. These studies indicate the capability of WAAM, representing a promising technology in modern manufacturing practices; however, it still lacks in-depth research and quality assessment standards to be adopted globally to realize the many advantages of WAAM process.

4 Conclusion

In this study, ER70S-6 wire was deposited using robotic-WAAM under various metal transfer modes with bead-on-plate trials, followed by fabricating multi-bead and multilayered structures in pulse transfer mode.

Metal transfer modes show significant influence on bead geometric features, dilution, microhardness, and microstructure. A low-level deposition current resulted in higher hardness in all transfer modes, while an increase of current decreased the average hardness. Each transfer mode showed distinct hardness profiles at various current levels. The global trend of hardness decreased from top to bottom in bead-on-plate deposits. The short/spray transfer mode exhibits lowest dilution for low and intermediate current, while it escalates at high current value. Pulse and double pulse transfer modes show comparatively higher dilution for low and intermediate current levels; however, they demonstrate comparatively stable and controlled dilution, indicating a better arc stability.

The interaction between the hatch distance and current have significant effects on the bead formation in multi-track deposition. The unfavorable combination of these parameters resulted in valleys and uneven surfaces between the adjacent beads. However, an optimization level exists for appropriate overlapping; for instance, 160 A current and 3 mm hatch distance resulted in a comparatively smoother surface.

The microstructure of bead-on-plate trials consists of a finer lamellar morphology at low current level which tends to form polygonal and columnar grains with explicit grain coarsening when the current is increased to intermediate and high levels. Similarly, the microstructure of thin wall showed a slight anisotropy in the building direction, with a mixture of plate-like and randomly oriented cementite lamellae, partially forming spheroidite morphology in the top section of the wall. In the middle section, the microstructure changed to a coarse and elongated ferritic structure, while the bottom represented a coarse polygonal microstructure. Moreover, the cubic structure showed acicular ferrites at the upper zone with the presence of some allotriomorphic ferrites in the middle and upper zones. The heat effected zone consisted of equiaxed polygonal ferrite with small pearlite islands at grain boundaries. Very small pores were observed in the thin wall, while the cubic structure showed a more homogeneous microstructure with much lower porosity compared to thin wall. The microstructural morphology, phase orientation and the presence of porosity were further verified by the SEM analysis. The hardness in thin wall decreased from top to the middle and then slightly increased near the bottom zone with small fluctuations in the remelt and HAZ. On the other hand, the cubic structure showed a relatively uniform hardness profile.

Funding Open access funding provided by Alma Mater Studiorum - Università di Bologna within the CRUI-CARE Agreement.

Declarations

Conflict of interest On behalf of all authors, the corresponding author states that there is no conflict of interest.

Ethical approval The authors state that the research did not involve vulnerable participants, minors, clinical patients, human tissue, animals, human biological material, and genetically modified organisms.

Consent to participate The authors understand that my manuscript and associated personal data will be shared with Research Square for the delivery of the author dashboard.

Consent for publication The authors agree with the Copyright Transfer Statement.

References

1. Newman ST, Zhu Z, Dhokia V, Shokrani A (2015) Process planning for additive and subtractive manufacturing technologies. CIRP Ann 64(1):467–470. https://doi.org/10.1016/j.cirp.2015.04.109
2. Svetlizky D, Das M, Zheng B, Vyatskikh AL, Bose S, Bandyopadhyay A, Schoenung JM, Lavernia EJ, Eliaz N (2021) Directed energy deposition (ded) additive manufacturing: physical characteristics, defects, challenges and applications. Mater Today 49:271–295. https://doi.org/10.1016/j.mattod.2021.03.020
3. Holliday DB (1993) Gas-Metal Arc Welding. In: Olson DL, Siewert TA, Liu S, Edwards GR (eds) Welding, Brazing, and Soldering. ASM International, Michigan, pp 180–185
4. Key JF (1993) Arc Physics of Gas-Tungsten Arc Welding. In: Olson DL, Siewert TA, Liu S, Edwards GR (eds) Welding, Brazing, and Soldering. ASM International, Michigan, pp 30–35
5. Alberti EA, Bueno BMP, D'Oliveira ASCM (2016) Additive manufacturing using plasma transferred arc. Int J Adv Manuf Technol 83(9–12):1861–1871. https://doi.org/10.1007/s00170-015-7697-7
6. Pant H, Anisha A, Ganga SG, Utkarsh C, Amir S, Patterson AE (2023) Applications of wire arc additive manufacturing (waam) for aerospace component manufacturing. Int J Adv Manuf Technol 127:4995–5011. https://doi.org/10.1007/s00170-023-11623-7
7. Omiyale BO, Olugbade TO, Abioye TE, Farayibi PK (2022) Wire arc additive manufacturing of aluminium alloys for aerospace and automotive applications: a review. Mater Sci Technol 38(7):391–408. https://doi.org/10.1080/02670836.2022.2045549
8. Laghi V, Gasparini G (2023) Explorations of efficient design solutions for wire-and-arc additive manufacturing in construction. Structures 56:104883. https://doi.org/10.1016/j.istruc.2023.104883
9. Davis AE, Breheny CI, Fellowes J, Nwankpa U, Martina F, Ding J, Machry T, Prangnell PB (2019) Mechanical performance and microstructural characterisation of titanium alloy-alloy composites built by wire-arc additive manufacture. Mater Sci Eng A 765:138289. https://doi.org/10.1016/j.msea.2019.138289
10. Ng CH, Bermingham MJ, Kent D, Dargusch MS (2021) High stability and high strength β-titanium alloys for additive manufacturing. Mater Sci Eng A 816:141326. https://doi.org/10.1016/j.msea.2021.141326
11. Kennedy JR, Davis AE, Caballero AE, Williams S, Pickering EJ, Prangnell PB (2021) the potential for grain refinement of wire-arc additive manufactured (waam) ti-6al-4v by zrn and tin inoculation. Addit Manuf 40:101928. https://doi.org/10.1016/j.addma.2021.101928
12. Çam G (2022) Prospects of producing aluminum parts by wire arc additive manufacturing (WAAM). Mater Today 62:77–85. https://doi.org/10.1016/j.matpr.2022.02.137
13. Gierth M, Philipp H, Yarop A, Jonas S, Bergmann JP (2020) Wire arc additive manufacturing (WAAM) of aluminum alloy almg5mn with energy-reduced gas metal arc welding (GMAW). Materials 13:2671
14. Su C, Chen X, Gao C, Wang Y (2019) Effect of heat input on microstructure and mechanical properties of al-mg alloys fabricated by waam. Appl Surf Sci 486:431–440. https://doi.org/10.1016/j.apsusc.2019.04.255
15. Hassel T, Carstensen T (2020) Properties and anisotropy behaviour of a nickel base alloy material produced by robot-based wire and arc additive manufacturing. Weld World 64(11):1921–1931. https://doi.org/10.1007/s40194-020-00971-7
16. Tanvir ANM, Ahsan RU, Ji C, Hawkins W, Bates B, Bong Kim D (2019) Heat Treatment effects on Inconel 625 components fabricated by Wire + arc additive manufacturing (WAAM)—Part 1: microstructural characterization. Int J Adv Manuf Technol 103:3785–3798
17. Yildiz AS, Davut K, Koc B, Yilmaz O (2020) wire arc additive manufacturing of high-strength low alloy steels: study of process parameters and their influence on the bead geometry and mechanical characteristics. Int J Adv Manuf Technol 108:3391–3404. https://doi.org/10.1007/s00170-020-05482-9
18. Rodrigues TA, Duarte VR, Tomás D, Avila JA, Escobar JD, Emma Rossinyol N, Schell TG (2020) In-situ strengthening of a high strength low alloy steel during wire and arc additive manufacturing (WAAM). Addit Manuf 34:101200. https://doi.org/10.1016/j.addma.2020.101200
19. Wu B, Pan Z, Ding D, Cuiuri D, Li H, Jing Xu, Norrish J (2018) A review of the wire arc additive manufacturing of metals: properties, defects and quality improvement. J Manuf Process 35:127–139. https://doi.org/10.1016/j.jmapro.2018.08.001
20. Jackson MA, Van Asten A, Morrow JD, Min S, Pfefferkorn FE (2016) A comparison of energy consumption in wire-based and powder-based additive-subtractive manufacturing. Proc Manuf 5:989–1005. https://doi.org/10.1016/j.promfg.2016.08.087
21. Cunningham CR, Flynn JM, Shokrani A, Dhokia V, Newman ST (2018) Invited review article: strategies and processes for high quality wire arc additive manufacturing. Addit Manuf 22:672–686. https://doi.org/10.1016/j.addma.2018.06.020
22. Tang HP, Qian M, Liu N, Zhang XZ, Yang GY, Wang J (2015) Effect of powder reuse times on additive manufacturing of ti-6al-4v by selective electron beam melting. JOM 67(3):555–563. https://doi.org/10.1007/s11837-015-1300-4
23. Iván T, Paskual A, Álvarez P, Suárez A (2018) Study on arc welding processes for high deposition rate additive manufacturing. Proc CIRP 68:358–362. https://doi.org/10.1016/j.procir.2017.12.095
24. Baier D, Bachmann A, Zaeh MF (2020) Towards wire and arc additive manufacturing of high-quality parts. Proc CIRP 95:54–59. https://doi.org/10.1016/j.procir.2020.01.180
25. Filippov A, Shamarin N, Moskvichev E, Savchenko N, Kolubaev E, Khoroshko E, Tarasov S (2020) Heat input effect on microstructure and mechanical properties of electron beam additive manufactured (EBAM) Cu-7.5wt.%Al Bronze. Materials 14:6948. https://doi.org/10.3390/ma14226948
26. Xian G, Jeong Mok O, Lee J, Cho SM, Yeom J-T, Choi Y, Kang N (2022) Effect of Heat Input on Microstructure and

mechanical property of wire-arc additive manufactured Ti-6Al-4V Alloy. Weld World 66:847–861. https://doi.org/10.1007/s40194-021-01248-3
27. Wang T, Zhang Y, Zhihong Wu, Shi C (2018) Microstructure and properties of die steel fabricated by waam using h13 wire. Vacuum 149:185–189. https://doi.org/10.1016/j.vacuum.2017.12.034
28. Rafieazad M, Ghaffari M, Nemani AV, Nasiri A (2019) Microstructural evolution and mechanical properties of a low-carbon low-alloy steel produced by wire arc additive manufacturing. Int J Adv Manuf Technol 105:2121–2134. https://doi.org/10.1007/s00170-019-04393-8
29. Lin Z, Goulas C, Ya W, Hermans MJM (2019) Microstructure and mechanical properties of medium carbon steel deposits obtained via wire and arc additive manufacturing using metal-cored wire. Metals 9:673. https://doi.org/10.3390/met9060673
30. Le VT, Mai DS, Doan TK, Paris H (2021) Wire and arc additive manufacturing of 308L stainless steel components: optimization of processing parameters and material properties. Eng Sci Technol Int J 24:1015–1026. https://doi.org/10.1016/j.jestch.2021.01.009
31. Wang L, Xue J, Wang Q (2019) Correlation between arc mode, microstructure, and mechanical properties during wire arc additive manufacturing of 316l stainless steel. Mater Sci Eng A 751:183–190. https://doi.org/10.1016/j.msea.2019.02.078
32. Veiga F, Suárez A, Aldalur E, Bhujangrao T (2021) Effect of the metal transfer mode on the symmetry of bead geometry in WAAM aluminum. Symmetry 13:1245. https://doi.org/10.3390/sym13071245
33. Panchenko O, Kurushkin D, Mushnikov I, Khismatullin A, Popovich A (2020) A high-performance waam process for al–mg–mn using controlled short-circuiting metal transfer at increased wire feed rate and increased travel speed. Mater Des 195:109040. https://doi.org/10.1016/j.matdes.2020.109040
34. Nguyen L, Buhl J, Bambach M (2020) Multi-bead overlapping models for tool path generation in wire-arc additive manufacturing processes. Procedia Manufacturing 47:1123–1128. https://doi.org/10.1016/j.promfg.2020.04.129
35. Ramos-Jaime D, Juárez IL, Perez P (2013) Effect of process parameters on robotic GMAW bead area estimation. Proc Technol 7:398–405. https://doi.org/10.1016/j.protcy.2013.04.050
36. Amrit Raj P, Mukherjee M, Raja M, Kundu S, Chatterjee A (2022) Development of near homogeneous properties in wire arc additive manufacturing process for near-net shaped structural component of low-carbon steel. Proc Inst Mech Eng 236:3497–3511
37. Campana G, Fortunato A, Ascari A, Tani G, Tomesani L (2007) The influence of arc transfer mode in hybrid laser-mig welding. J Mater Process Technol 191(1–3):111–113. https://doi.org/10.1016/j.jmatprotec.2007.03.001
38. KOBELCO Welding Handbook, KOBE STEEL LTD., 2022, page 71. https://www.kobelco.co.jp/english/welding/files/handbook.pdf.
39. Saleh B, Fathi R, Yinbao Tian N, Radhika JJ, Ma A (2023) Fundamentals and advances of wire arc additive manufacturing: materials, process parameters, potential applications, and future trends. Arch Civil Mech Eng 23:96. https://doi.org/10.1007/s43452-023-00633-7
40. Vishwanatha HM, Rao RN, Maiya M, Kumar P, Gupta N, Saxena KK, Vijayan V (2024) Effects of arc current and travel speed on the processing of stainless steel *via* wire arc additive manufacturing (WAAM) process. J Adhesion Sci Technol 38:2222–2239. https://doi.org/10.1080/01694243.2023.2289770
41. Badoniya P, Srivastava M, Jain PK (2024) Parametric influence and effect of cooling channel on bead geometry profiles of ER70S-6 manufactured using wire arc additive manufacturing. Mater Today. https://doi.org/10.1016/j.matpr.2024.04.076
42. Badoniya P, Srivastava M, Jain PK, Rathee S (2024) Parametric investigation on wire arc additive manufacturing of ER70S-6 low-carbon steel for fabrication of thick-walled parts. J Adhesion Sci Technol 38:1925–1952. https://doi.org/10.1080/01694243.2023.2275823
43. Novelino ALB, Carvalho GC, Ziberov M (2022) Influence of waam-cmt deposition parameters on wall geometry. Adv Indus Manuf Eng 5:100105. https://doi.org/10.1016/j.aime.2022.100105
44. Kamble G, Rao RV (2022) Investigation on effects of parameters of GMAW process on bead geometry, hardness and microstructure of AISI 410 steel weldments. Adv Mater Process Technol 8:2450–2464. https://doi.org/10.1080/2374068X.2021.1912537
45. Barath Kumar MD, Arivazhagan N, Tofil S, Andersson J, Kozak J, Manikandan M (2024) Influence of pulsed current GTAW-WAAM process parameters on the single layer bead geometry and multi bead multi-layer deposition of a nickel-based superalloy. Mater Today Commun 39:108824. https://doi.org/10.1016/jj.mtcomm.2024.108824
46. Zhang D, Prasad A, Bermingham MJ, Todaro CJ, Benoit MJ, Patel MN, Qiu D, StJohn DH, Qian Ma, Easton MA (2020) Grain refinement of alloys in fusion-based additive manufacturing processes. Metall and Mater Trans A 51(9):4341–4359. https://doi.org/10.1007/s11661-020-05880-4
47. Nguyen VT, Minh PS, Uyen TMT, Do TT, Ngoc HVT, Le MT, Nguyen VTT (2023) WAAM technique: process parameters affecting the mechanical properties and microstructures of low-carbon steel. Metals 13:873. https://doi.org/10.3390/met13050873
48. Ding D, Pan Z, Cuiuri D, Li H (2015) A multi-bead overlapping model for robotic wire and arc additive manufacturing (waam). Robot Comp Integr Manuf 31:101–110. https://doi.org/10.1016/j.rcim.2014.08.008
49. Ou W, Knapp GL, Mukherjee T, Wei Y, DebRoy T (2021) An improved heat transfer and fluid flow model of wire-arc additive manufacturing. Int J Heat Mass Transf 167:120835. https://doi.org/10.1016/j.ijheatmasstransfer.2020.120835
50. Li Y, Sun Y, Han Q, Zhang G, Horváth I (2018) Enhanced beads overlapping model for wire and arc additive manufacturing of multi-layer multi-bead metallic parts. J Mater Process Technol 252:838–848. https://doi.org/10.1016/j.jmatprotec.2017.10.017
51. Elsokaty A, Oraby O, Sadek S, Salem HG (2022) Influence of wire arc additive manufacturing beads' geometry and building strategy: mechanical and structural behavior of ER70S-6 prismatic blocks. J Manuf Mater Process 7:3. https://doi.org/10.3390/jmmp7010003
52. Ron T, Levy GK, Dolev O, Leon A, Shirizly A, Aghion E (2020) The effect of microstructural imperfections on corrosion fatigue of additively manufactured ER70S-6 alloy produced by wire arc deposition. Metals 10:98. https://doi.org/10.3390/met10010098
53. Vahedi Nemani A, Ghaffari M, Nasiri A (2020) On the post-printing heat treatment of a wire arc additively manufactured ER70S part. Materials 13:2795. https://doi.org/10.3390/ma13122795
54. Haden CV, Zeng G, Carter FM, Ruhl C, Krick BA, Harlow DG (2017) Wire and arc additive manufactured steel: tensile and wear properties. Addit Manuf 16:115–123. https://doi.org/10.1016/j.addma.2017.05.010
55. Abbaszade M, Bol N, Kara OE, Sen AA, Yılmaz O (2022) On the mechanical behavior and microstructural characterization of wire + arc additive manufacturing of Mn-Si based steel alloy (ER70S-6). J Addit Manuf Technol 2(2):648. https://doi.org/10.18416/JAMTECH.2212648
56. Nagasai B, Prasanna SM, Balasubramanian V (2023) Effect of interlayer delay on microstructure and bead geometry of wire arc additive manufactured low carbon steel components. Int J Interactive Design Manuf 17:939–946. https://doi.org/10.1007/s12008-022-01009-6
57. Rodrigues TA, Duarte V, Miranda RM, Santos TG, Oliveira JP (2019) Current status and perspectives on wire and arc additive

manufacturing (WAAM). Materials 12(7):1121. https://doi.org/10.3390/ma12071121
58. Jafari D, Vaneker THJ, Gibson I (2021) Wire and arc additive manufacturing: opportunities and challenges to control the quality and accuracy of manufactured parts. Mater Design 202:109471. https://doi.org/10.1016/j.matdes.2021.109471
59. Shukla V, Kumar V, Dixit A (2023) Microstructural characteristics and tensile properties of ER70S-6 manufactured by robotic CMT Wire-and-arc additive manufacturing. Mater Today. https://doi.org/10.1016/j.matpr.2023.02.011
60. Ascari A, Lutey AHA, Liverani E, Fortunato A (2020) Laser directed energy deposition of bulk 316L stainless steel. Lasers Manuf Mater Process 7:426–448. https://doi.org/10.1007/s40516-020-00128-w
61. Shassere B, Nycz A, Noakes MW, Masuo C, Sridharan N (2019) Correlation of microstructure and mechanical properties of metal big area additive manufacturing. Appl Sci 9:787. https://doi.org/10.3390/app9040787
62. Rafieazad M, Nemani AV, Ghaffari M, Nasiri A (2021) On microstructure and mechanical properties of a low-carbon low-alloy steel block fabricated by wire arc additive manufacturing. J Mater Eng Performance 30:4937–4945. https://doi.org/10.1007/s11665-021-05568-9
63. Anwar AM, Ali RM, Imam M, Pandit D, Jha KK, Kesharwani R, Kar M, Chinthapenta V (2023) Comparison of the microstructures and mechanical properties in the overlapping region of low carbon steel additive bead fabricated by WAAM and FSP. Metall Mater Trans A 54:869–895. https://doi.org/10.1007/s11661-022-06934-5
64. Mohammadi J, Iman Dashtgerd A, Riahi R, Mostafaei A (2024) Pulsed gas metal arc additive manufacturing of low-carbon steel: microstructure observations and mechanical properties. Mater Today Commun 38:107637. https://doi.org/10.1016/j.mtcomm.2023.107637
65. Warsi R, Kazmi KH, Chandra M (2022) Mechanical properties of wire and arc additive manufactured component deposited by a CNC controlled GMAW. Mater Today 56:2818–2825. https://doi.org/10.1016/j.matpr.2021.10.114
66. Peng D, Jones R, Ang ASM, Michelson A, Champagne V, Birt A, Pinches S, Kundu S, Alankar A, Singh RRK (2022) Computing the durability of WAAM 18Ni 250 maraging steel specimens. Fatigue Fract Eng Mater Struct 45:3535–3545. https://doi.org/10.1111/ffe.13828
67. Peng D, Champagne VK, Ang ASM, Birt A, Michelson A, Pinches S, Jones R (2023) Computing the durability of WAAM 18Ni-250 maraging steel specimens with surface breaking porosity. Crystals 13:443. https://doi.org/10.3390/cryst13030443
68. Webster GA, Alireza B, Shakil SI, Riyanka R, Kathleen C, Krishnamurthy A, Zekriardehani S et al (2023) Wire arc additive manufactured AWS ER100S-G steel: very high cycle fatigue characterization. Eng Failure Anal 154:107721. https://doi.org/10.1016/j.engfailanal.2023.107721
69. Peng D, Rhys J, Andrew SM, Victor C, Aaron B, Alex M (2022) A numerical study into the effect of machining on the interaction between surface roughness and surface breaking defects on the durability of WAAM Ti-6Al-4V parts. Metals 12:1121. https://doi.org/10.3390/met12071121
70. Astarita A, Campatelli G, Corigliano P, Epasto G, Montevecchi F, Scherillo F, Venturini G (2021) Microstructure and mechanical properties of specimens produced using the wire-arc additive manufacturing process. Proc Inst Mech Eng 235(10):1788–1798. https://doi.org/10.1177/0954406219883324
71. Joosten S Printing a stainless-steel bridge: An exploration of structural properties of stainless-steel additive manufactures for civil engineering purposes, Master thesis. http://repository.tudelft.nl.
72. Deb R, Wei JS, Zuback T, Mukherjee JW, Elmer JO, Milewski AM, Beese A, De W-HA, Zhang W (2018) Additive manufacturing of metallic components – process, structure and properties. Prog Mater Sci 92:112–224. https://doi.org/10.1016/j.pmatsci.2017.10.001
73. Williams SW, Martina F, Addison AC, Ding J, Pardal G, Colegrove P (2016) Wire + arc additive manufacturing. Mater Sci Technol 32(7):641–647. https://doi.org/10.1179/1743284715Y.0000000073